

1 **MoonIndex, an Open-Source Tool to Generate Spectral Indexes for the Moon**  
2 **from M<sup>3</sup> Data**

3 **Javier Eduardo Suárez-Valencia<sup>1</sup>, Angelo Pio Rossi<sup>1</sup>, Francesca Zambon<sup>2</sup>, Cristian Carli<sup>2</sup>,**  
4 **and Giacomo Nodjoui<sup>1</sup>**

5 <sup>1</sup>School of Science, Constructor University, Bremen, Germany, <sup>2</sup>INAF-Istituto Nazionale di  
6 Astrofisica, Italy.

7 Corresponding author: Javier Eduardo Suárez Valencia ([jsuarezvalencia@constructor.university](mailto:jsuarezvalencia@constructor.university))

8

9 This manuscript is an article published in the journal Earth and Space Science.

## 10 Abstract

11 Spectral indexes are tools widely used to analyze the composition of planetary surfaces. Many  
12 indexes have been formulated over the years to map the lunar surface, but there is no unified  
13 database for them. In this work we describe an Open-Source Python package called *MoonIndex*,  
14 that recreates thirty-eight indexes compiled from the literature, using data from the Moon  
15 Mineralogy Mapper (M<sup>3</sup>). The processing started with the filtering of the data cubes to reduce  
16 the noise, the continuum of the spectrum was then removed using a convex hull or a second-and-  
17 first-order fit method. Later, the indexes were calculated, following as possible the original  
18 formulations. The results on spectral indexes calculated before the continuum removal were  
19 similar to those of the original formulations. Conversely, the results obtained for spectral indexes  
20 calculated after the continual removal were not always coherent. Some indexes, like the band  
21 depth, are especially sensitive to the removal method, as well as the derived band areas and  
22 asymmetries. We also recreated RGB composite maps, our results highlight the compositional  
23 patterns in a similar way as the ones in the literature, even if the color ramps can differ. The  
24 products of *MoonIndex* are open, ready for interpretation, versatile, consistent, and cross-  
25 comparable.

## 26 Plain Language Summary

27 Spectral indexes are parameters defined from the characteristics of reflectance spectra, and they  
28 are useful to investigate the spectral properties of a surface and to retrieve mineralogical  
29 properties of a planetary body. They can reveal the presence of specific minerals in rocks,  
30 indicate mineralogical variations from different units, highlight physical properties of a surface,  
31 or show the effect of the exposure to the space environment. For the Moon, several spectral  
32 indexes have been formulated over time using data from many spacecraft, but no unified  
33 database is available. In this work, we created an open-source Python package called  
34 *MoonIndex*, which recreates thirty-eight indexes to study the lunar surface. The indexes were  
35 collected from the literature, and our results achieved various levels of fidelity. Some of the  
36 indexes we calculated exactly reproduce those found in the literature, while in other cases, index  
37 calculations differ due to processing constraints or due to missing information in the original  
38 formulations, such as the continuum removal method used, or the band operations conducted to  
39 create the indexes. *MoonIndex* is a reliable and versatile tool to approach the compositional  
40 analysis of the lunar surface.

## 41 1 Introduction

42 The surface of the Moon has a limited mineralogical diversity, it has been broadly  
43 divided into two types of terrains, the “highlands” which are anorthosite-rich and relatively light-  
44 toned, and “maria”, dark-toned plains of effusive lavas enriched in mafic and opaque minerals  
45 (Taylor, 1976, Hiesinger and Head, 2006). In the highlands, the dominant minerals are calcium  
46 plagioclases (Taylor, 1972, Warren and Korotev, 2022), while in the maria mafic compositions  
47 become important showing higher abundances of clinopyroxene (CPX), orthopyroxene (OPX),  
48 and olivine (Agrell et al., 1970, Albee, 2003). The clear definition of the lunar mineralogy has  
49 been driven by the samples returned by space missions (Prissel and Prissel, 2021), but due to  
50 their limited coverage of the lunar surface, the use of remote sensing techniques is still the only  
51 way to assess the mineralogy of the Moon at a global level. In this respect, the formulation and  
52 use of spectral indexes is a straightforward way to approach and visualize the mineralogical  
53 diversity of the Moon. In this study we present and describe *MoonIndex*, an open-source Python

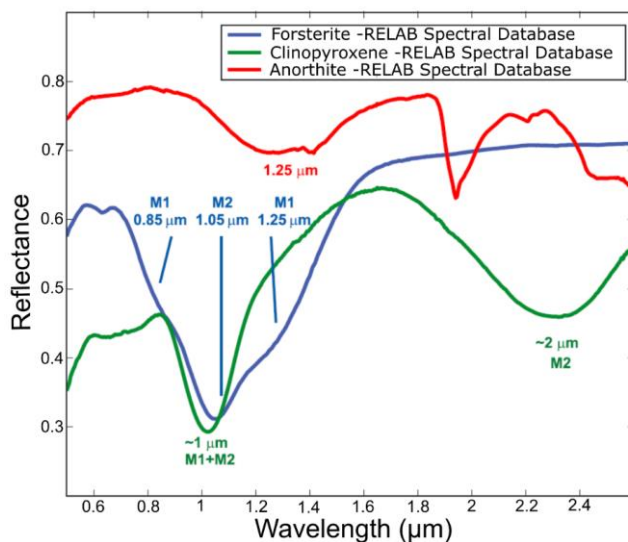
54 library that generates spectral indexes derived from the data of the Moon Mineralogy Mapper  
55 ( $M^3$ ).

56 After the end of the Apollo missions, the exploration of the Moon shifted towards the use  
57 of remote sensing spacecraft around the Moon. These orbiters allowed global and long-lasting  
58 surveys of the surface, including the study of mineralogical and elemental variations across lunar  
59 terrains. The first spacecraft with this purpose was Clementine. It was launched in 1994 and it  
60 was equipped with the Ultraviolet/Visible (UV/Vis) and the Near-Infrared CCD (NIR) cameras  
61 (Nozete, 1995), which combined 11 filters between 300 nm and 2700 nm. This spectral range  
62 was selected to obtain information suitable for the recognition of the dominant minerals on the  
63 surface of the Moon (**Figure 1**). Clementine was followed by the Lunar Prospector, launched in  
64 1998, it allowed the derivation of potassium, thorium, and iron maps of the surface from its  
65 gamma-ray spectrometer (Lawrence et al., 1998). The Selenological and Engineering Explorer  
66 (SELENE/Kaguya) was launched in 2007 (Sasaki et al. 2003), it carried the first hyperspectral  
67 sensor orbiting the Moon, its Spectral Profiler consisted of 296 bands between 522 nm and 2600  
68 nm. Shortly after, in 2008, the Chandrayaan-I spacecraft was launched, and its payload included  
69 hyperspectral sensor called the Moon Mineralogy Mapper ( $M^3$ ) (Pieters et al., 2009, Green et al.,  
70 2011).  $M^3$  acquired data in the spectral range between 430 nm and 3000 nm, similarly to  
71 Kaguya/Spectral Profiler, but with a higher spatial resolution. It operated in two spectral  
72 sampling modes: the “Target Mode”, characterized by a spectral sampling of 10 nm, with a total  
73 of 256 channels; and the “Global Mode”, reaching a spectral sampling of 20 nm in the shorter  
74 wavelengths and 40 nm in longer ones, adding up to 85 channels (Green et al., 2011). In both  
75 cases the spatial resolution is around 110 meters/pixel for the products of the first orbital period,  
76 and around 240 meters/pixel for the products of a second one. The spectral cubes usually cover  
77 long swaths of the lunar surface. Due to the limited amount of the targeted mode products and  
78 the almost total coverage of the global mode ones, we decided to optimize the workflow for the  
79 latter.

## 80 1.1 Lunar mineralogical diversity

81  $M^3$  acquired data in the spectral interval between 0.45  $\mu\text{m}$  and 3  $\mu\text{m}$ , corresponding to the  
82 range where the major mafic minerals and water ice exhibit clear absorption features. **Figure 1**  
83 shows an example of some minerals with scientific interest on the Moon (pyroxene, plagioclase,  
84 and olivine) showing specific spectral signatures in the visible-near infrared range (Arnold et al.,  
85 2016). Olivine presents three absorption features ranging between 0.85  $\mu\text{m}$  and 1.3  $\mu\text{m}$ , this is  
86 attributable to the presence of  $\text{Fe}^{2+}$  within the M1 and M2 octahedra sites (e.g. Burns 1993),  
87 creating a wide absorption feature around 1.1  $\mu\text{m}$ . Nevertheless, changes in the composition of  
88 the olivine can slightly shift the position of the band center of the absorption, with a shift towards  
89 longer wavelengths with increasing fayalite, i.e.  $\text{Fe}^{2+}$  (e.g. Burns, 1993; Sunshine and Pieters,  
90 1998). Grain size also has a role in the position of the band center, as smaller particles will shift  
91 its location to shorter wavelengths (e.g. King and Ridley, 1987). Pyroxene exhibits two strong  
92 absorptions centered at 1  $\mu\text{m}$  and 2  $\mu\text{m}$ , respectively. These absorptions are mainly the result of  
93 crystal field transitions of  $\text{Fe}^{2+}$  cations in the M1 and M2 octahedral sites, however, the presence  
94 of different abundances of  $\text{Ca}^{2+}$  (and related  $\text{Mg}^{2+}$ ) also influence the absorption bands of  
95 pyroxenes (Burns, 1993; Klima et al. 2011). In fact, pyroxene with a larger amount of  $\text{Fe}^{2+}$  and  
96  $\text{Ca}^{2+}$  show band center positions shifted towards longer wavelengths (Klima et al., 2007, 2011)

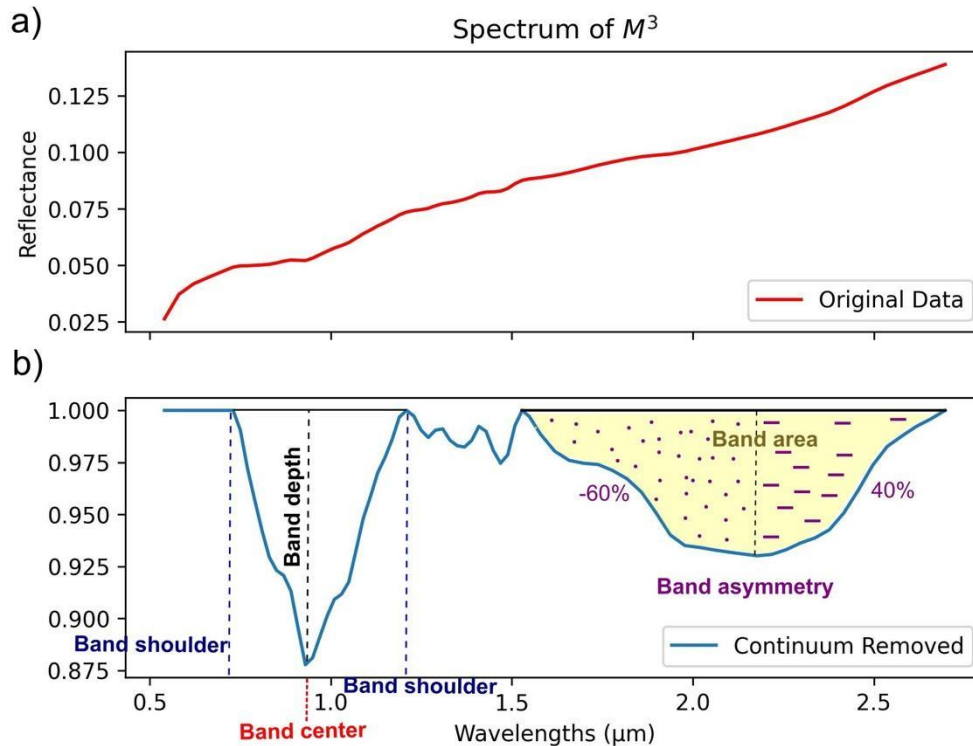
97 as well as extreme composition shows wider 1.0  $\mu\text{m}$  and weak or absent 2.0  $\mu\text{m}$  band. Different  
 98 from the other major minerals, plagioclase has a higher reflectance and is almost featureless in  
 99 the near-infrared (NIR), even if small amount of  $\text{Fe}^{2+}$  produce an absorption band around 1.3  
 100  $\mu\text{m}$ , which is not easily recognizable in the data of  $\text{M}^3$  (e.g. Ohtake et al., 2009, Cheek et al.,  
 101 2013, Serventi, 2013). To properly analyze the plagioclase composition, one should rely on  
 102 thermal infrared (TIR) data, such as that obtained by the Diviner instrument onboard the Lunar  
 103 Reconnaissance Orbiter (LRO)(Lucey et al., 2021). An additional shallow absorption band  
 104 centered around 3  $\mu\text{m}$ , which is associated to hydrated minerals, has been identified by  $\text{M}^3$  data  
 105 (Pieters et al., 2009). As well as an absorption feature between 1.5  $\mu\text{m}$  and 3  $\mu\text{m}$ , related to the  
 106 presence of spinels (Pieters et al., 2014, Moriarty et al., 2023). In general, a spectrum that shows  
 107 an absorption feature at 2  $\mu\text{m}$  indicates the presence of pyroxene, one with a stronger signal at 1  
 108  $\mu\text{m}$  implies the presence of olivine, and a spectrum with shallow absorption in both regions  
 109 represents an absence of the mafic minerals, and thus the abundance of plagioclase.



110  
 111 **Figure 1: Spectral signatures of the main mineral species on the lunar surface. The**  
 112 **three absorption features of olivine are shown in blue (M1, M2, M3). The two absorptions**  
 113 **of pyroxene are shown in green (M1, M2). The high reflectance spectrum of plagioclase**  
 114 **is shown in red, showing the occasional absorption feature at 1.3  $\mu\text{m}$ . Modified from Arnold**  
 115 **et al. (2016).**

116 Since the lunar surface is a mixture of minerals, the actual spectrum is more complex  
 117 than the ones obtained from single species (**Figure 2a**). Other factors also add a layer of  
 118 complexity. Instrumental errors need to be considered, as well as the overall signature of the  
 119 regolith (Green et al., 2011). But the bigger factor is that the lunar spectra show an overall  
 120 positive and steep slope (**Figure 2a**), this effect is known as spectral reddening and is the result  
 121 of space weathering. This alteration is produced by the combined action of solar wind, cosmic  
 122 radiation, and micrometeoroid bombardment. This produces nanophase iron particles,  
 123 responsible for the increased spectral slope, a reduction of the reflectance, and the weakening of  
 124 some absorption bands (Hapke, 2001; Xu et al., 2023). Spectral reddening hinders the absorption

125 band analysis; therefore, it is necessary to remove the spectral slope. A typical way to remove the  
126 spectral slope effects is to apply a continuum removal (**Figure 2b**).



127

128 **Figure 2: a) Example of a reflectance spectrum extracted from  $M^3$  data before**  
129 **continuum removal, showing the steep slope of the continuum. b) Same spectrum after the**  
130 **continuum removal. The main spectral parameters are indicated in the plot. The band**  
131 **center is the wavelength at the minimum point of the absorption, the band depth is the**  
132 **value at the minimum, the band shoulders limit the absorption, the band area is the total**  
133 **coverage of the absorption, and the asymmetry measures the distribution of the area at**  
134 **each side of the minimum as a percentage.**

135 1.3 Techniques to exploit spectral data

136 Several approaches can be used to analyze spectral data acquired by remote sensing  
137 instruments. A common method is the use of spectral indexes, those are specific combinations of  
138 bands, or band operations, that highlights a specific portion of the spectrum and thus a  
139 mineralogical composition (e.g. Montero et al., 2023). The definition of the indexes is supported  
140 by an analysis of the shape of the identified absorption bands (through the band centers, band  
141 depths, bands shoulders, band areas, spectral slopes, etc) (**Figure 2b**); or by operating over  
142 specific spectral bands, like calculating spectral ratios. In some cases indexes are presented as  
143 RGB composites, false-colored images that are created by combining three indexes in the red,

144 green, and blue channels. This allows an easier visualization of the results by comparing several  
145 indexes at the same time and supporting the interpretation (Liu and Mason, 2009).

146 Other techniques can also be applied to spectral datasets. The Modified Gaussian Model  
147 (MGM) (Sunshine et al., 1990; Clenet, 2009) allows the retrieval of mineralogical information  
148 from a representative spectrum. Furthermore, spectral unmixing models (e.g. Adams et al., 1993;  
149 Farrand et al., 2006; Horgan et al., 2022), and radiative transfer models (Corley et al., 2018),  
150 focus on the reconstruction of synthetic spectra using the Hapke reflectance model (Hapke,  
151 1993), which computes the expected reflectance of minerals from their chemical and  
152 crystallographic properties. Although the spectral indexes technique does not easily allow an  
153 absolute measurement of mineral abundances in complex spectra, it is still the most flexible, as  
154 many types of indexes can be created. This allows a targeted survey of desired minerals and an  
155 easy analysis of their spatial relationships with other ones, including minor species like spinel.  
156 For the previous reasons, we focused our work on the compilation of spectral indexes present in  
157 the literature for the Moon and within the spectral range of  $M^3$ , to later recreate them on the  
158 Open-Source programming language Python.

## 159 1.2 Spectral indexes from the literature provided by *MoonIndex*

160 The spectral parameters are intrinsic to the mineral species, which means spectra are  
161 comparable regardless of the planetary body. Many parameters were defined in the laboratory  
162 (e.g. Adams and Filice, 1967; Adams, 1974; Karr, 1975), and were later applied to the Moon. A  
163 detailed list of all the spectral indexes considered in this work is shown in **Table 1**. Spectral  
164 indexes depend on the characteristics of the spectra considered, for this reason, literature  
165 provides a large and evolving number of parameters. Therefore, no unified database of spectral  
166 indexes for the Moon is present. Nevertheless, some works went a long way listing important  
167 indexes. Zambon et al. (2020) describes eleven indexes suitable for being derived from the data  
168 of  $M^3$ . These indexes focus on the band centers and band depths around 1  $\mu\text{m}$  and 2  $\mu\text{m}$ , which  
169 help on the identification of mafic minerals; the spectral slope, which is a way to measure the  
170 maturity of the surface; a Clementine-like color composite map (Red: 750 nm/540 nm, Green:  
171 750 nm/1000 nm, Blue:540 nm/750 nm), suitable to identify regions enriched in mafic minerals  
172 (with different enrichment on iron or titanium), plagioclase and glass-bearing materials (Lucey et  
173 al., 2000).

174 The rest of the collected indexes were thought of for specific cases. Wu et al. (2012)  
175 updated the FeO and TiO parameters formulated by Lucey et al. (2000). Horgan et al. (2014)  
176 used the band area and asymmetry to highlight different mineral and glass compositions. Corley  
177 et al. (2018) defined a simple band ratio to highlight the presence of olivine, and Bretzfelder et  
178 al. (2020) made an RGB composite based on the integrated band depth (IBD) around 1  $\mu\text{m}$  and 2  
179  $\mu\text{m}$ , and the band depth at 1.9  $\mu\text{m}$  to create a contrast between olivine and the two types of  
180 pyroxenes. Besse et al. (2011) also used the integrated band depth (IBD) to differentiate between  
181 pulses of lava floods. Finally, Pieters et al. (2014) and Moriarty et al. (2023) used band ratios of  
182 non-continuum removed spectra designed to detect spinel and anorthosite. Finally, we adapted  
183 three other indexes for this work, the band area and asymmetry at 2  $\mu\text{m}$ , and a chromite  
184 parameter following the formulation of Moriarty et al, 2023.

Parameter Name	Abrev. Name	Formulation	Interpretation	Source
Reflectance at 540 nm	R540	$R540$	High values (Higher than 0.03) → bright fresh material, plagioclase. Low values (Lower than 0.03) → dark terrain, pyroxene, and other mafic minerals.	Adams and McCord (1971)
Band center at 1 μm	BCI	$BCI = \min \sim \left( \frac{R1000nm}{R_c1000nm} \right)$ $R_c = \text{Removed continuum spectrum}$	Compositional variations of the principal mineralogical phases (pyroxenes, olivines, and plagioclases). Low-Ca pyroxenes have values lower than 0.99, high-Ca pyroxenes have values higher than 0.99.	Adams (1974)
Band center at 2 μm	BCII	$BCII = \min \sim \left( \frac{R2000nm}{R_c2000nm} \right)$	If the band center is shifted to lower wavelengths, it may show abundance of low-Ca pyroxene. Low-Ca pyroxenes have values lower than 2.15, high-Ca pyroxenes have values higher than 2.15.	Adams (1974)
Band depth at 1 μm	BDI	$BDI = 1 - \frac{R1000nm}{R_c1000nm}$	Abundance of the principal mineralogical phases and their grain sizes, also abundance of opaque phases. Values depend on the minerals involved and their proportions.	Adams (1974)
Band depth at 2 μm	BDII	$BDII = 1 - \frac{R2000nm}{R_c2000nm}$	Abundance of the principal mineralogical phases and their grain sizes, also abundance of opaque phases. Values depend on the minerals involved and their proportions.	Adams (1974)
Spectral slope at 1 μm	SS	$Sl = \frac{R(\text{Max shoulder BCI}) - R540nm}{(\text{Wave}(\text{Max shoulder BCI}) - 540nm) * R540nm}$	Low values → fresh terrains, dark terrain. High values → older terrains, space weathering.	Hazen et al. (1978)
Clementine-like red channel	Clem RED	$ClemRED = \frac{R750nm}{R540nm}$	High values imply low titanium regions, or high glass contents.	Lucey et al. (2000)
Clementine-like green channel	Clem GREEN	$ClemGREEN = \frac{R750nm}{R1000nm}$	High values show enrichment of iron in the surface, and mafic minerals.	Lucey et al. (2000)

Clementine-like blue channel	Clem BLUE	$ClemBLUE = \frac{R540nm}{R750nm}$	Higher values imply high titanium content and bright slopes.	Lucey et al. (2000)
Band depth at 1.9 $\mu\text{m}$	BD1900	$BD1900 = 1 - \frac{R1900nm}{R_c1900nm}$	Highlights differences in mafic compositions when combined with IBDI and IBDII.	Bretzfelder et al. (2020)
Integrated band depth at 1 $\mu\text{m}$	IBDI	$IBDI = \sum_{n=0}^{26} \left[ 1 - \frac{R(789nm + 20n)}{R_c(789nm + 20n)} \right]$	It shows high values when olivine and pyroxene are present. Values depend on the minerals involved and their proportions.	Bretzfelder et al. (2020)
Integrated band depth at 2 $\mu\text{m}$	IBDII	$IBDII = \sum_{n=0}^{21} \left[ 1 - \frac{R(1658nm + 40n)}{R_c(1658nm + 40n)} \right]$	It shows high values when pyroxene is present. Values depend on the minerals involved and their proportions.	Bretzfelder et al. (2020)
Band area at 1 $\mu\text{m}$	BAI	$BAI = \sum_{n=0}^{La} \left( 1 - \frac{R(ICnm + 20n)}{R_c(ICnm + 20n)} \right) * SR$  <i>IC = Channel where the absorption begins</i> <i>SR = Spectral resolution</i> <i>La = Amount of channels covered</i>	Useful to differentiate between mineral species. Bigger areas imply the presence of more mafic minerals. When plotted against the band center gives information about the mixture of mafic minerals.	Cloutis et al. (1986), Zhang et al. (2016)
Band area at 2 $\mu\text{m}$	BAIL	$BAIL = \sum_{n=0}^{La} \left( 1 - \frac{R(ICnm + 40n)}{R_c(ICnm + 40n)} \right) * SR$	Useful to differentiate between mineral species. Bigger areas imply the presence of more mafic minerals. When plotted against the band center gives information about the mixture of mafic minerals.	This paper, Zhang et al. (2016)
Band asymmetry at 1 $\mu\text{m}$	ASYI	$ASYI = \frac{BAIR - BAIL}{BAIR + BAIL} * 100$  <i>BAIR = Right side of the band area</i> <i>BAIL = Left side of the band area</i>	Useful to identify glass-bearing mixtures with high asymmetries. Asymmetries higher than 15 points to the presence of glass. When plotted against the band center gives information about the mixture of mafic minerals.	Cloutis et al. (1986)
Band asymmetry at 2 $\mu\text{m}$	ASYII	$ASYII = \frac{BAIIR - BAIIL}{BAIIR + BAIIL} * 100$	Useful to identify glass-bearing mixtures with high asymmetries. When plotted against the band center gives information about the mixture of mafic minerals.	This paper

Olivine parameter	Ol	$Ol = \left( \frac{R1699}{0.1 * R1050 + 0.1 * R1210 + 0.4 * R1329 + 0.4 * R1469} \right) - 1$	A higher value implies a major abundance of olivine. This index is only indicative, to properly quantify the amounts of olivine, the use of a radiative transfer model is suggested.	Corley et al. (2018)
Spinel ratio	Sp1	$Sp1 = \frac{R1450nm}{R1750nm}$	A higher value implies a major abundance of spinel. This index is only indicative, it is not intended to be a quantitative tool.	Pieters et al. (2014)
Spinel ratio	Sp2	$Sp2 = \frac{\left( \frac{R1250nm - R750nm}{500} \right) * 1350 + R1250nm}{R2600nm}$	A higher value implies a major abundance of spinel. This index is only indicative, it is not intended to be a quantitative tool.	Moriarty III et al. (2022)
Pyroxene ratio	Px	$Px = \frac{R700nm + R1200nm}{R950nm}$	A higher value implies a major abundance of pyroxene. This index is only indicative, it is not intended to be a quantitative tool.	Pieters et al. (2014)
Pure anorthosite ratio	An	$Px = \frac{R1000nm + R1500nm}{R1250nm}$	A higher value implies a major abundance of anorthosite. This index is only indicative, it is not intended to be a quantitative tool.	Pieters et al. (2014)
Band depth at 950 nm	BD950	$BD950 = 1 - \frac{R950nm}{R_c950nm}$	While combined with other indexes to create the RGB6 composite is useful to study lunar maria. A higher value implies the presence of mafic minerals.	Besse et al. (2011)
Band depth at 1.05 μm	BD1050	$BD1050 = 1 - \frac{R950nm}{R_c950nm}$	While combined with other indexes to create the RGB6 composite is useful to study lunar maria. A higher value implies the presence of mafic minerals.	Besse et al. (2011)
Band depth at 1.25 μm	BD1250	$BD1250 = 1 - \frac{R1250nm}{R_c1250nm}$	While combined with other indexes to create the RGB6 composite is useful to study lunar maria. A higher value implies the presence of mafic minerals.	Besse et al. (2011)
Reflectance at 1.58 μm	R1580	$R1580nm$	While combined with other indexes to create the RGB7 composite is useful to study lunar maria.	Besse et al. (2011)
Iron oxide parameter	Fe	$Fe = - \arctan \arctan \left( \frac{\left( \frac{R918nm}{R757nm} \right) - 1.19}{R757nm - 0.06} \right)$	Higher values imply the presence of iron. The percentage of FeO in weight can be derived from the parameter: $wt\%FeO = 8.878 * Fe^{1.8732}$	Wu et al. (2012)

Titanium parameter	Ti	$Ti = \arctan \arctan \left( \frac{\left( \frac{R561nm}{R757nm} \right) - 0.71}{R757nm - 0.07} \right)$	Higher values imply the presence of titanium. The percentage of FeO in weight can be derived from the parameter: $wt\%FeO = 2.6275 * Ti^{4.2964}$	Wu et al. (2012)
Chromite parameter	Cr	$Cr = \frac{\left( \frac{R1350 - R750}{600} \right) * 1500 + R1350}{R2750}$	Higher values imply the presence of chromite. This index is only indicative, it is not intended to be a quantitative tool.	This paper
<b>RGB composite Name</b>	<b>Abrev. Name</b>	<b>Formulation</b>	<b>Interpretation</b>	<b>Source</b>
RGB Clementine-like color composite	Clem	R: ClemRED, G: ClemGREEN, B: ClemBLUE.	Red channel → low titanium regions, or high in glass content (see the highlands, pyroclastic deposits). Green channel → amount of iron in the surface, mafic minerals. Blue channel → high titanium. Lunar surface maturity.	Lucey et al. ( 2000)
Color composite 1	RGB 1	R: SS, G: BDI, B: BDII.	When red dominates, space weathering is major, blue/green zones correspond to less mature terrains.	Zambon et al. (2020)
Color composite 2	RGB 2	R: SS, G: R540, B: BCII.	Blue areas are characterized by high iron/titanium, red zones are a lack of that.	Zambon et al. (2020)
Color composite 3	RGB 3	R: SS, G: R540, B: BDI.	This RGB combination gives information on terrain maturity and reflectance.	Zambon et al. (2020)
Color composite 4	RGB4	R: BCI, G: BCII, B: BAI.	Pyroxene rich material is seen in blue/yellow/green, glass and olivine in pink/yellow, plagioclase in red.	Horgan et al. (2014)
Color composite 5	RGB5	R: ASYI, G: BCII, B: BAI.	Pink and yellow show glass-bearing mixtures, blue a mixture of pyroxenes.	Horgan et al. (2014)
Color composite 6	RGB6	R: BD950, G: BD1050, B: BD1250.	Blue could imply the presence of olivine, red/purple the presence of Mg-pyroxene, yellow the presence of Ca-pyroxene.	Besse et al. (2011)

Color composite 7	RGB7	R: IBDI, G:IBDII, B: R1580.	Red is olivine rich, highlands rich in plagioclase appear blue, low-Ca pyroxene appear in green and yellow.	Besse et al. (2011)
Color composite 8	RGB 8	R: BD1900, G: IBDII, B:IBDI.	Dark blue corresponds to olivine signatures, cyan to clinopyroxene.	Bretzfelder et al. (2020)
Color composite of spinel	Spanpx	R :Px, G: Sp2, B: An.	Pyroxene in red, presence of spinel in green, and anorthosite in blue and yellow.	Moriarty III et al. (2022)

186

187

188

**Table 1: List of spectral indexes collected in the literature. A total of 28 single-band parameters and 10 RGB composites were implemented.**

## 2. Data

As our goal was to generate a set of consistent spectral indexes, we opted for optimizing the tool for the global mode captures of  $M^3$ , in this way we always worked with the same spectral sampling and similar spatial resolutions. We selected the data from the Planetary Data System (PDS) (Malaret et al., 2011), using the PDS Geosciences Node Lunar Orbital Data Explorer (LODE) search tool.

### 2.1 Data formats

$M^3$  data is available as cubes with an IMG file extension, each cube is a three-dimensional array of data, which stores spatial information in a two-dimensional plane, and spectral information in the third dimension. Other additional files contain ephemerides, geometries, calibration data, and metadata. To map-project the data it is necessary to download the geometric data of the radiance image and the derived reflectance cube, the latter being the one used for the retrieval of the spectral parameters. The reflectance cubes available in the PDS have 83 bands, missing the first two bands, corresponding to  $0.46 \mu\text{m}$  and  $0.5 \mu\text{m}$ . The reflectance data in the PDS is already calibrated for thermal and photometrical anomalies (Clark et al., 2011; Lundeen et al., 2011). Other authors have noted problems with this correction, especially after the  $2 \mu\text{m}$  range, where the thermal emission of the lunar surface should be considered (Bandfield et al., 2018; Li and Milliken, 2017). In this work we use the reflectance cubes of the PDS, but further processed products can also be ingested to *MoonIndex*. The spatial resolution of the global mode data used in this paper is around 110 meters/pixel, while the spectral sampling is variable, being  $0.02 \mu\text{m}$  between  $0.5 \mu\text{m}$  to  $1.5 \mu\text{m}$ , and  $0.04 \mu\text{m}$  between  $1.5 \mu\text{m}$  and  $3 \mu\text{m}$ . Global mode cubes cover a substantial portion of the lunar surface, so one or two cubes are usually enough to study medium-sized landforms. On the global mode, the data is captured at full resolution, and is afterwards downsized to reduce it to the desired resolution.  $M^3$  captured data intermittently across two orbital periods, usually with high solar zenith angles (Green et al. 2011), as a result, there are not many locations covered by more than one or two cubes taken at different times.

$M^3$  data is affected by some artifacts, making it difficult to develop general procedures to remove or improve these issues (Green et al., 2011). In particular, all  $M^3$  files display vertical stripes due to thermal issues with the instrument. The stripes are present in all wavelengths, but their intensity varies from cube to cube. We also detected an anomalous increase in reflectance from right to left in some cubes. This effect is particularly strong at longer wavelengths, affecting the band depth, area, and asymmetry (Green et al., 2011). The photometric correction of the cubes is not reliable for incidence angles higher than 70 degrees, which especially affect steep slopes on craters. Finally, there are some cubes taken in the same area that are not correctly projected with respect to each other, this may be a problem with the SPICE information of the data (Acton et al., 2016). Although the mentioned artifacts reduce the quality of the information, almost every cube still has plenty of data that can be analyzed.

## 2.2 Case study regions

All the indexes collected and formulated in this work are applicable to any location on the lunar surface. Here, as a study case, we compare our results with those of three other authors that also focused on spectral indexes (**Figure 3**).

### 2.2.1 Apollo Basin

The Apollo basin (36.1°S 151.8°W) was the target of Zambon et al. (2020). It is a large multiring impact basin within the northern part of the South Pole Aitken basin (SPA) (Moriarty and Pieters, 2018). It has an estimated age of 3.98 Ga (Ivanov et al., 2018) and was later filled by basaltic flood lavas. The Apollo basin has a big geomorphological and compositional diversity (Ivanov et al., 2018, Potter et al., 2018), most of the zone is dominated by highlands terrains, but a large basaltic flood is emplaced at the center of the basin. This diversity makes it a good target to test the variability of the spectral parameters. Zambon et al. (2020) used the band center, depth, and spectral slope to study the mineralogical composition of the region, we will compare our results for these same parameters. We used the reflectance cube M3G20090813T213525.

### 2.2.2 Vallis Alpes

Vallis Alpes (49°N, 3°E.) was studied by Bretzfelder et al. (2020). The Vallis Alpes and Montes Alpes are landforms located in the northern rim of the Imbrium basin, they are northeast trending structures, including a central linear rille and parallel mountain ranges at both sides of it. The mountains are probably ejecta blocks of the Imbrium impact, which according to Klima et al. (2011) are enriched in low-Ca pyroxene. Bretzfelder et al. (2020) identified olivine outcrops in the surface using the integrated band depths and the band depth at 1.9  $\mu\text{m}$ , suggesting the presence of plutonic rocks excavated from the lower crust (Shearer et al. 2015). We recreated these parameters to identify the presence of olivine in the region. The reflectance image used for this target is M3G20090608T125102.

### 2.2.3 Aristarchus crater

The Aristarchus Crater (23.4°N, 47.2°W) was analyzed by Horgan et al. (2014). It is a well-preserved Copernican complex crater, it shows high albedo and sharp morphologies, which correspond to impact products (Mustard et al., 2011). The structure of its ejecta is clearly visible, including several types of impact melt, basement rocks and structural patterns. Horgan et al. (2014) used the band centers, areas and asymmetries to study and classify the ejecta and glass bearing lithologies around the crater. The reflectance M<sup>3</sup> cube used for this target is M3G20090209T054031.

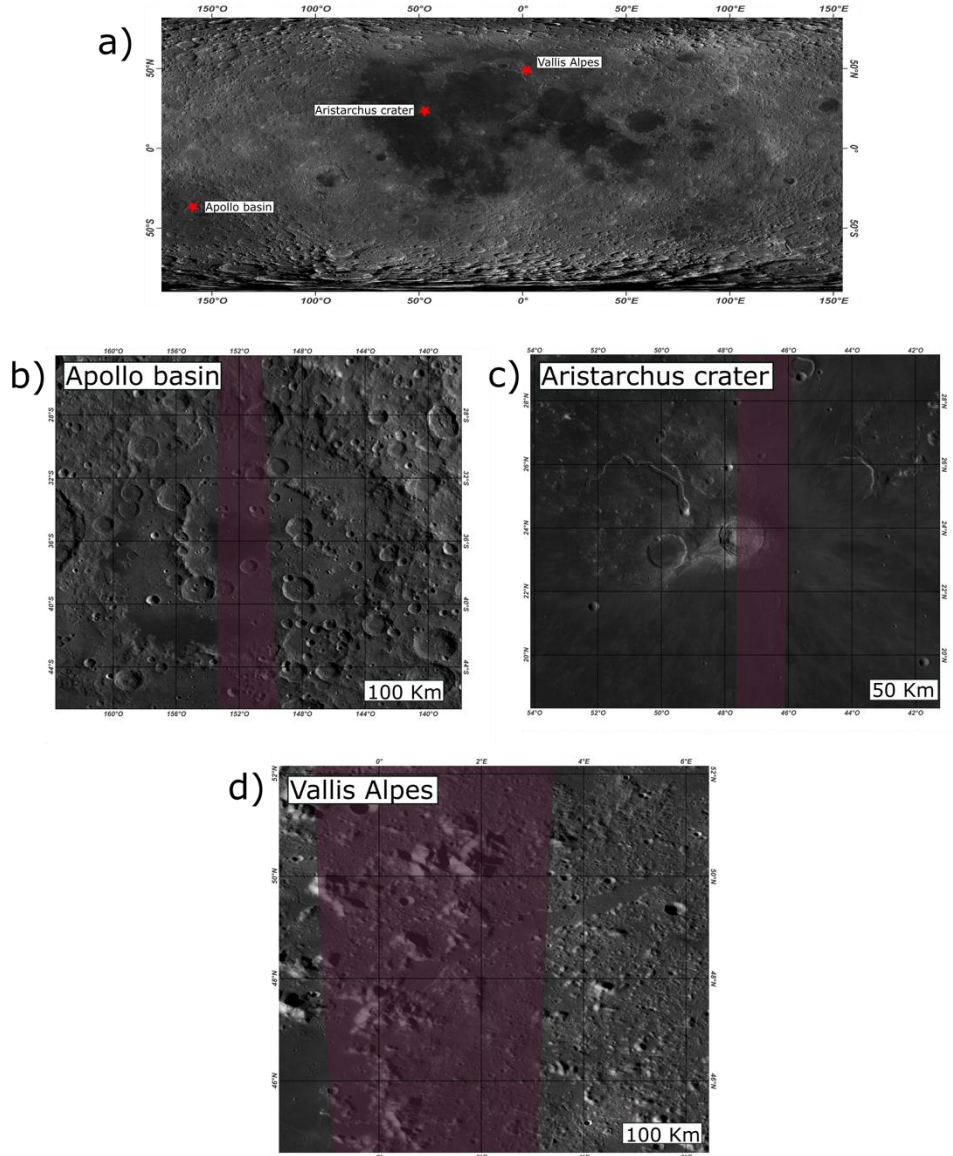


**Figure 3: a) Regions selected to test the MoonIndex tool. b) Apollo Basin, a large impact structure in the South Polar Aitken basin (SPA), target of Zambon et al. (2020). c) Aristarchus crater, a Copernican impact structure enriched in glasses, target of Horgan et al. (2014). d) Vallis Alpes, a linear rille in the rim of the Imbrium basin, target of Bretzfelder et al. (2020).**

### 3 Methods

The use of other software is necessary before and after the application of *MoonIndex*. An important step to properly use remote sensing images is the spatial projection of the data, which locates the images on the surface of a planet. For planetary bodies, this process is challenging, and has been optimized before in software like the Integrated Software for Imagers and Spectrometers (ISIS) (Laura et al., 2023). For this reason, we did not recreate this step within the Python workflow. Then, *MoonIndex* can

be applied to map-projected  $M^3$  reflectance cubes. As for the indexes derived from our tool, we strongly recommend their use with geospatial software such as QGIS or ArcGIS, which are well-optimized for high level remote sensing data interpretation. The whole workflow applied is summarized in **Figure 4**.

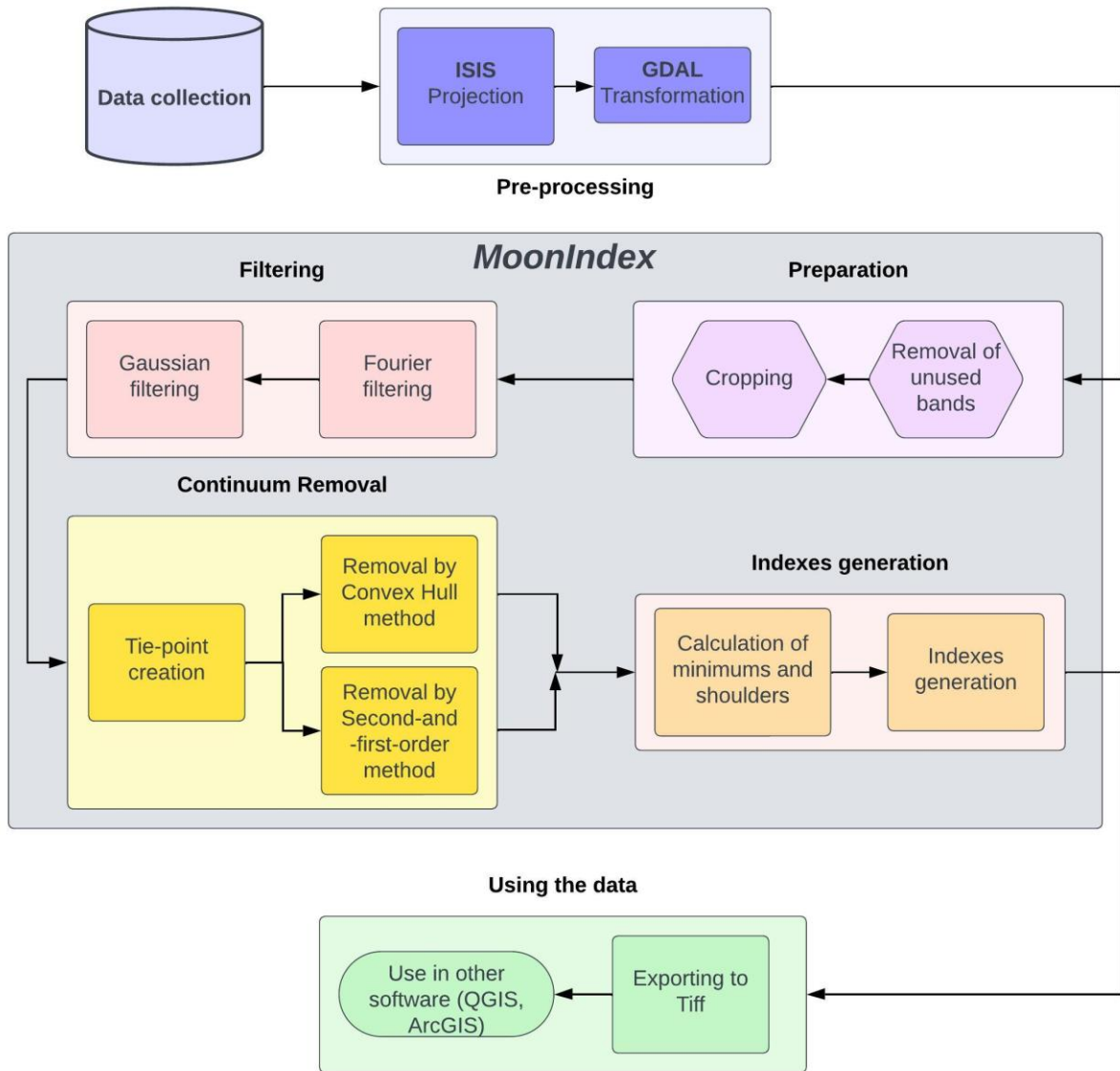


**Figure 4: Flow-chart of the full procedure to create spectral indexes using *MoonIndex*.**

### 3.1 Preprocessing

To process  $M^3$  cubes through *MoonIndex*, the user first needs to map-project them and change their format to Tiff/Geotiff using ISIS and the Geospatial Data Abstraction Library (GDAL) (Rouault et al., 2023). The first step is the ingestion of the data to ISIS,

the importing command of ISIS only accepts the radiance product of  $M^3$ , so we performed a change in the associated LBL file of the radiance cube to use the reflectance data (e.g., Figuera et al., 2018). The modification consists in changing the name of the radiance cube by the one of the reflectance cube in the “`^RDN_IMAGE`” parameter under the “/\* Description of Radiance-corrected image file \*/” section of the LBL file. This tricks ISIS to accept the reflectance cube, and to continue the pre-processing. As the data of  $M^3$  usually covers a substantial portion of the Moon, sometimes it is necessary to reduce the extent of the cube, this is usually necessary when the data comprise the poles. The polar region covered by the cube can be cropped to a smaller size in ISIS. Then, we geographically projected the cube to a pre-defined coordinate system. After the projection, the format of the data was changed from CUB to TIF using GDAL. At this point, the data is ready to be ingested on the tool. The commands used in this step can be found in **Text S1**.

### 3.2 Data processing using *MoonIndex*

The *MoonIndex* tool is designed to automatically work, after an initial configuration of the input and output paths. The indexes are calculated from a set of Python functions developed in this work, which are optimized for the technical characteristics of  $M^3$ . The workflow can be divided into three main stages (**Figure 4**): filtering, continuum removal (when needed), and indexes generation. We used Python libraries that are produced/written to work with spatial imagery data, like *xarray* (Hoyer and Joseph, 2017), *openCV* (Bradsky, 2000), and *rasterio* (Gillies and others, 2013). And we also used common operational libraries like *numpy* (Harris et al., 2020), and plotting ones like *matplotlib* (Hunter, 2007). A detailed description of the libraries is found in **Text S2**.

#### 3.2.1 Cube adjustments

Some minor corrections are needed before working with the data. The first two bands of the reflectance cube do not contain spectral information, so they are removed, this means that the initial band of the data is  $0.54 \mu\text{m}$ . The pixels with no-data values all are reassigned to zero, to avoid problems in the processing. Due to the  $M^3$  observation strategy, a large part of the cubes is acquired from north to south pole, increasing the file dimension and making the data processing difficult (Green et al., 2011). For this reason, a specific tool to resize the data is fundamental for easier data processing. In this regard, we develop a function dedicated to crop the data using the coordinates of the desired

regions (**Figure 5**). Nevertheless, the user can still opt to process the full cube by simply not using this function.

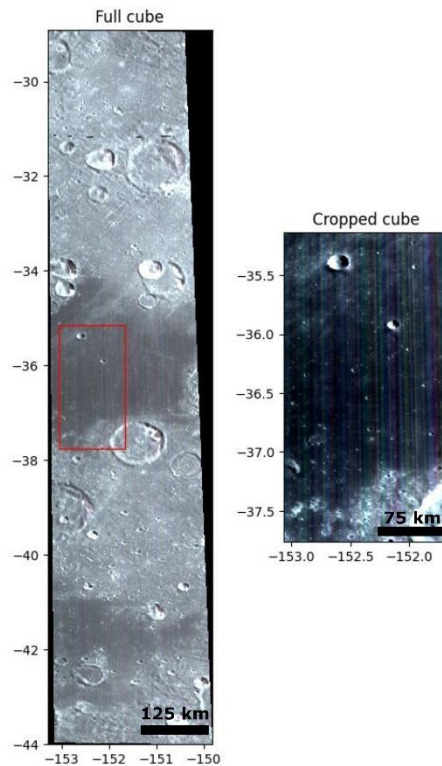


**Figure 5: Cropping function of the tool. M3 cubes are generally large, so the use of subsections when possible is recommended.**

### 3.2.2 Filtering

The striping of the cubes can disrupt the data, both the spectral profiles and the images for each wavelength have a periodic noise that makes interpretation more difficult (**Figure 6a**). Since no instrumental calibration is provided by the team of M<sup>3</sup>, we opted for filtering the data. Some of the recreated spectral indexes require operations over specific bands, so we did not applied processes that reduce the dimensions of the data, like the Minimum Noise Fraction (MNF) method used in M<sup>3</sup> cubes by Kodikara et al. (2015). Instead, we followed a simple two-step smoothing method proposed by Shkuratov et al. (2019), which consists of a Gaussian convolution followed by a Fourier filtering. After several attempts we obtained better results inverting the order of the filters, as less striping is visible after generating the indexes.

The Fourier filtering was computed individually for each band of the cube. The process starts by applying a 2D Fourier transform, the resulting image is in the Fourier or frequency domain, which shows the distribution of frequencies contained in the original spatial domain (Broughton & Bryan, 2018). In the Fourier domain, it is possible to identify some frequencies responsible for the vertical striping of the data, which horizontally cross the Fourier image at its center (**Figure 6b**). Once the position of the

stripes was identified, we applied a mask to the data, multiplying by zero the regions dominated by their frequencies (**Figure 6c**). The size of the mask corresponds to 60% of the width of the image, and 2% of its altitude; these measurements were established manually as it removes the major number of stripes without damaging the frequencies of the actual data, usually accumulated at the center of the Fourier image. The user has the possibility to change the size of the filter. Lastly, an inverse Fourier transform is applied to the masked images, recovering the filtered cube in the spatial domain. After the Fourier filtering, a simple 1D Gaussian filter is applied to the data, this time in the spectral dimension. This process smooths the spectral signatures of each pixel, allowing the identification of the main mineral absorption bands (**Figure 7a**). The filter is only applied between  $0.54\ \mu\text{m}$  and  $2.85\ \mu\text{m}$ , to avoid an undesired trend caused by the instrumental errors at longer wavelengths. As most of the minerals on the Moon have absorption bands in shorter wavelengths, we decided not to include those unfiltered last four bands. Finally, we examined that the filters do not affect the actual data. We generated ratioed images between the filtered and unfiltered cubes, and then checked that variations of over 2% were not made outside the location of the vertical stripes (**Figure 7b**).

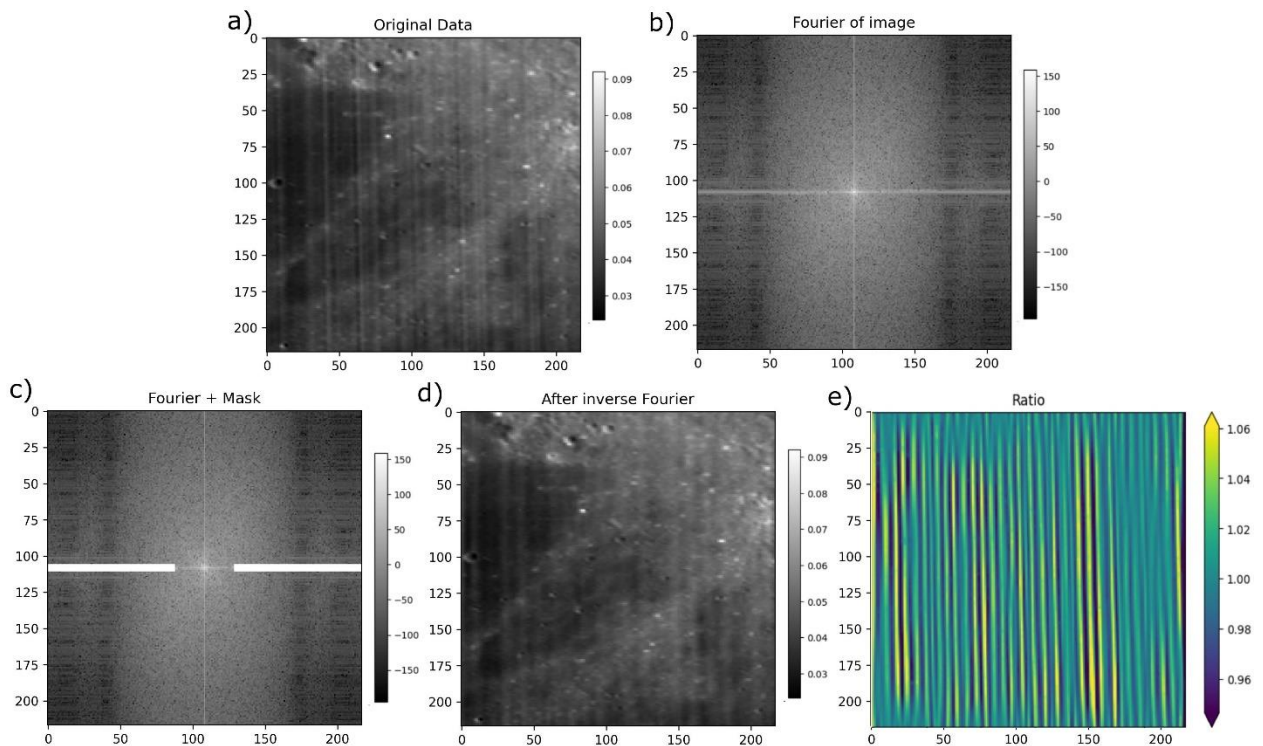


**Figure 6: Fourier filtering of the Apollo Basin cube, the gray scale ramp represents reflectance. a) Original data with the typical vertical striping of M<sup>3</sup>. b) Fourier image of the data, the strong horizontal line contains the frequencies of the vertical stripes. c) Filter applied to the data, the pixels inside the rectangles are multiplied by zero.**

d) Image after the filtering, showing a reduction in the number of vertical stripes. e) Ratio between the original image and the one after the fourier filtering.

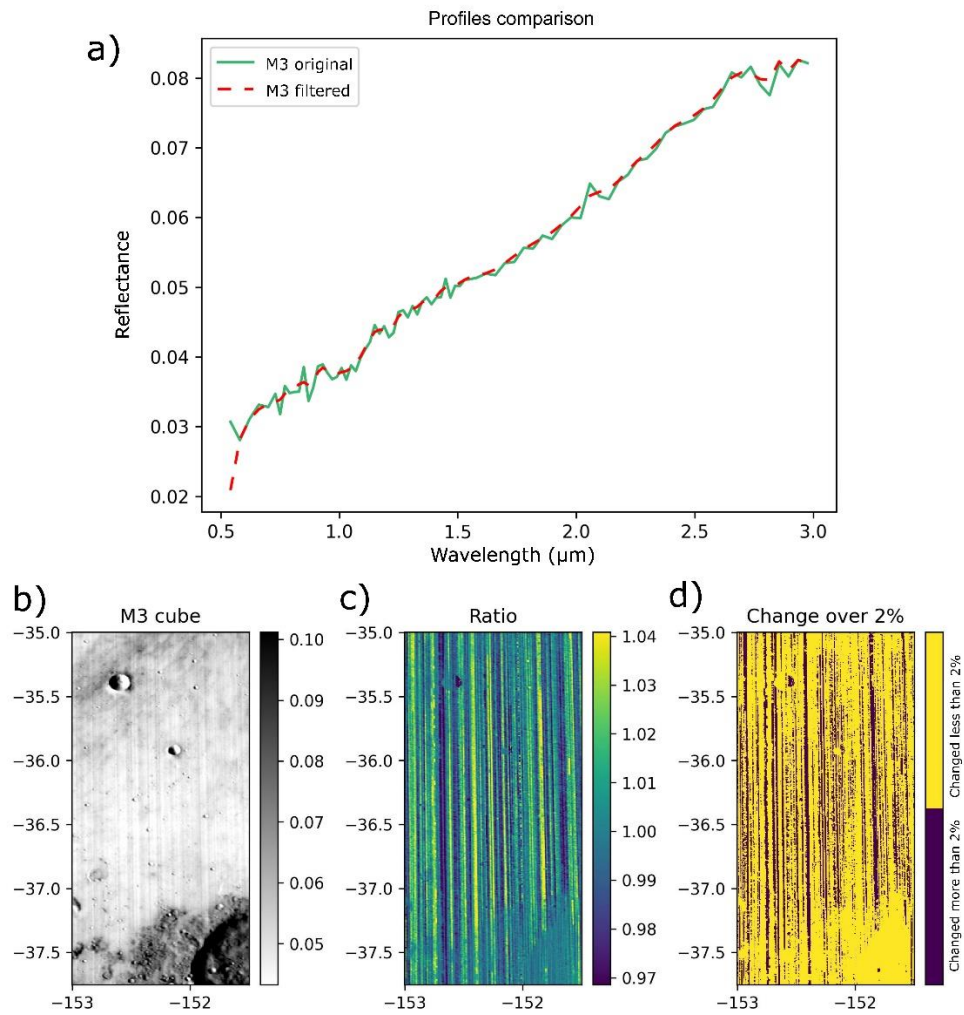


**Figure 7: a) Comparison of the spectral profiles before and after the Gaussian filter, the orange line is smoother and allows a better interpretation of the absorption bands. b) Images of the original cube, c) the ratio between the last and the Gaussian-filtered cube, d) and the location with changes over 2% on reflectance (black pixels). These images show the surface data is not affected by the filtering process.**

### 3.2.3. Continuum removal

Some indexes require a continuum removal of the spectrum to be performed. The continuum of a spectrum is considered the background absorption signal, which results from the interaction of several properties of the analyzed surface (e.g., Clark and Rush, 1984; Zhang et al., 2016). The continuum on the spectral signatures of M<sup>3</sup> is a positive slope that overlaps the relatively weak absorption of the minerals, it results from the combined signals of the lunar regolith and the products of space weathering. In the lunar case, a major contribution to the continuum is due to space weathering effects, which in

turn can be used to measure the maturity of the surface (Lucey et al., 2000). Even when the continuum plays a major role in  $M^3$  cubes, its removal uncovers the spectral properties of the minerals on the surface and allows the analysis of parameters related to absorption bands (**Figure 8**).

Several approaches have been used to remove the continuum of lunar spectra, we decided to implement two of these methods in *MoonIndex*. Since this process consist of removing the overall trend of the data, the most common approach in the literature involves calculating the continuum as a linear or polynomial fit between the first and last value of the spectrum, and then using it to divide the original data (e.g., McCord et al., 1972; Clark and Roush, 1984). Similarly to Zambon et al. (2020, and references therein), we applied a second-and-first-order fit method to remove the continuum of  $M^3$  data. By considering the spectral properties of the minerals on the lunar surface, the removing function was calculated independently for each absorption band. Around the 1  $\mu\text{m}$  band, a second order fit was used, and for the one around the 2  $\mu\text{m}$ , a linear fit function was applied. We named this approach as the “second-and-first-order fit method” in our tool (**Figure 8b**). Nevertheless, the polynomial order of this method can be modified for both absorption bands. The other approach implemented is the convex hull method (Graham, 1972), in this case, the continuum is calculated as the enveloping function of the spectral data, consisting of lines interpolated over every consecutive point of the spectrum. This method has the advantage of being completely independent of arbitrary limits for the absorption bands and that it highlights the shape of every absorption feature. We implemented this approach as the “convex hull method” in our tool (**Figure 8a**). Although the code is flexible by allowing the use of both continuum-removal methods, we recommend the convex-hull one, since its automatic detection of the band shoulders would work better in locations were the mineralogy differs from the typical plagioclase-pyroxene-olivine dominance (as the position of the band shoulders in the second-and-first-order fit method are fixed to the usual ranges of these minerals).

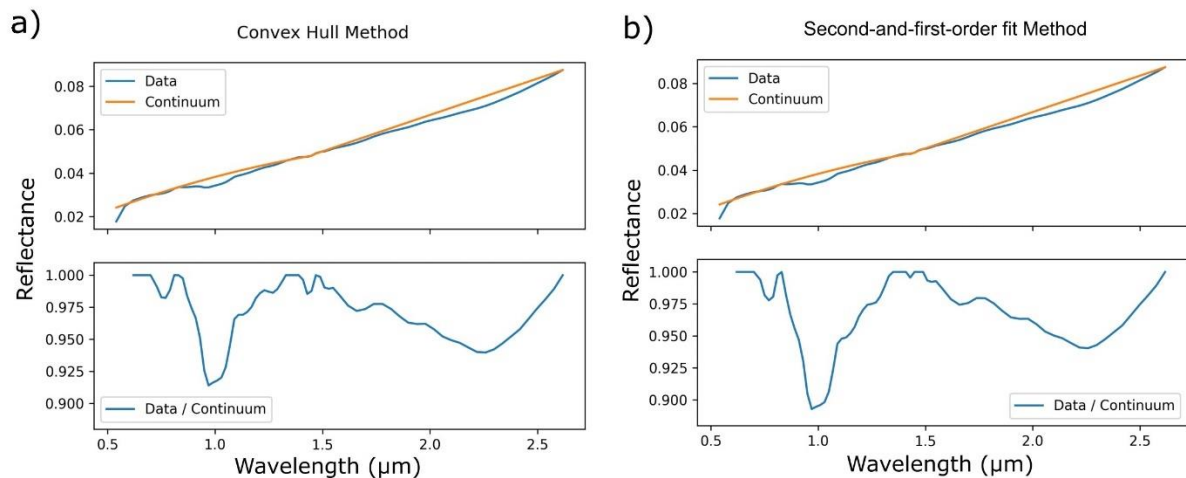


**Figure 8: Continuum removal methods applied by *MoonIndex*. a) Convex-hull method, it used an envelope around the vertex of the spectrum. b) Second-and-**

**first-order fit method, it used a second order polynomial around the 1  $\mu\text{m}$  absorption band, and a linear fit around the 2  $\mu\text{m}$  absorption band.**

An additional challenge was found when the spectra had a steep slope, this creates an effect where the local maximums are masked, especially near the right shoulder of the 1  $\mu\text{m}$  absorption band (also the left shoulder of the 2  $\mu\text{m}$  absorption band). This resulted in an incorrect calculation of the convex hull and the second-and-first-order fit methods, since the algorithm was not able to find the local maximum. To bypass this problem, we created a tie-point between 1 and 2  $\mu\text{m}$ , which is set to a higher value than the surrounding data, ensuring that the continuum removal process will count it as a maximum. This artificial point marks the closure of the absorption band at 1  $\mu\text{m}$  and the beginning of the one at 2  $\mu\text{m}$ , only when the spectral signature is too featureless to be detected. The position of the tie-point was defined as the most prominent peak of the difference between the original spectrum and its continuum, calculated with a linear fit between 1.02  $\mu\text{m}$  and 2.09  $\mu\text{m}$ . We selected this range since the absorption band at 1  $\mu\text{m}$  usually closes inside it.

### 3.2.4 Key parameters extraction

Once the continuum has been removed, the data is ready for the retrieval of spectral indexes. Two parameters were calculated first, the position of the minimum reflectance and the position of their two surrounding shoulders, for both the 1  $\mu\text{m}$  and 2  $\mu\text{m}$  bands. These parameters are key to calculate other indexes since they define the limits of the two main regions of mineralogical interest. The minimum is also used to derive the band depth, while the shoulders are necessary to calculate the band areas, which in turn allow the definition of the band asymmetries. The position of the minimum reflectance (or maximum absorption) is simply defined as the wavelength where the spectrum has its lower value, this is calculated independently for the 1  $\mu\text{m}$  and the 2  $\mu\text{m}$  band, being the tie-point the limit for both. The positions of the shoulders were defined as the first local maximums to the left and right of the band minimum. Since this operation is done after the removal of the continuum, the shoulders have values equal to one (**Figure 2**). Also, the data after 2.65  $\mu\text{m}$  was cut from all the spectra, so this value is set as the right shoulder of the 2  $\mu\text{m}$  band for every pixel.

Once the continuum removal was performed, we made a second-order polynomial fit around the minimums and maximums to further reduce the noise of the resulting indexes, this is done within a window from two wavelengths lower up to two wavelengths higher.

We established detection limits for the key parameters using thresholds for the band depths since it would not be accurate to analyze the absorption band if it is too shallow. Below the thresholds, the band center, depth, area, asymmetry, and derived parameters are not calculated. The definition of the limit was done using the cube for the Apollo Basin, since it contains several types of terrains, and thus is representative of the overall lunar mineralogy. The lowest meaningful detection would be around 0.005 since the level of the noise is typically lower than this value (**Figure S2**). However, a higher threshold was established using the distribution of the band depths at 1 and 2  $\mu\text{m}$ , we

choose a limit at 1.5 standard deviations to the left, that is 0.026 for the 1  $\mu\text{m}$  absorption, and 0.017 for the 2  $\mu\text{m}$  absorption. By doing a manual check of spectra with band depths below these values, we found that the absorption features are usually anomalous, and should not be computed (**Figure S3**). A total of 0.15% pixels were filtered for 1  $\mu\text{m}$ , and 0.35% at 2  $\mu\text{m}$  for the Apollo basin cube. By setting these limits it is possible that some true detections would be lost, especially for cubes with wider distributions or less mineralogical variation; nevertheless, most anomalous detections might be avoided, and the number of pixels removed below these limits is not substantial.

### 3.2.5 Indexes generation

A total of 28 indexes were reconstructed in this work. In **Table 1** we report the calculation of the parameters, their significance, and exemplary RGB composites that use them. We created Python functions that generate a raster for every index listed in **Table 1**.

Among the parameters, the ones done before the removal of the continuum consists of simple operations between bands. Those can be quickly calculated in Python after ingesting and filtering the data. As an example, the pyroxene ratio formulated by Pieters et al. (2014) was calculated as:

$$Px = \frac{R700 \text{ nm} + R1200 \text{ nm}}{R950 \text{ nm}} \quad (1)$$

Where, for example, R700 is the reflectance at 700 nm. A list with all the formulations can be found in **Table 1**. For the parameters done after the continuum removal, the calculation involves operations between the continuum and the spectrum. The band center and the band depth are defined as (Adams 1974):

$$BCI = \left( \frac{RB \text{ nm}}{RB_c \text{ nm}} \right) \quad (2)$$

$$BD = 1 - \frac{RB \text{ nm}}{RB_c \text{ nm}} \quad (3)$$

Where RB is the reflectance of the spectrum, and RBc the value of the continuum. The band area was calculated for the two main absorption bands at 1  $\mu\text{m}$  and 2  $\mu\text{m}$  with (Cloutis, 1986):

$$BA = \sum_{\square} \left( 1 - \frac{RB \text{ nm}}{RB_c \text{ nm}} \right) * SR \quad (4)$$

Where SR is the spectral sampling of the cube, and the summation is limited by the positions of the shoulders of the absorption bands. Finally, the asymmetry is calculated as the difference in the area between the right and left half of the absorption band (**Figure 2**). Given as a positive percentage when the asymmetry is higher to the right, and negative when it is higher to the left. A more complex index is the integrated

band depth (IBD) (Bretzfelder et al., 2020), that is the sum of the band depths at each point along the full extension of an absorption band. It was calculated as:

$$IBD = \sum_{\lambda} \left[ 1 - \frac{R(B nm + SR)}{RB_c(B nm + SR)} \right] \quad (5)$$

A few indexes were adapted in this work from previous authors. Horgan et al. (2014) evaded using the band area and asymmetry at 2  $\mu\text{m}$  since the absorption features of pyroxenes at longer wavelengths is not fully captured by the range of  $M^3$ . Nevertheless, we believe calculating them is still useful, so we use the same method as their counterparts at 1  $\mu\text{m}$ , closing the spectrum at 2.5  $\mu\text{m}$  to avoid hydroxyl absorptions at 2.8  $\mu\text{m}$  and the instrumental errors of the last channels. At last, we generated a chromite parameter. Since the reflectance spectrum of chromite is like the one of spinel, but with absorptions bands located at slightly longer wavelengths (Cloutis et al., 2004), we followed the approach of Moriarty et al. (2023) for spinel. The parameter is a ratio between an extrapolated value at 1.5  $\mu\text{m}$ , using the slope between 0.75  $\mu\text{m}$  and 1.3  $\mu\text{m}$ , and the reflectance value at 2.7  $\mu\text{m}$ . Like on the spinel parameter, this should highlight regions where the 2  $\mu\text{m}$  absorption is higher than usual. It is important to consider that the spectrum of both minerals is similar, so a unique parameter that differentiates between them is difficult to achieve.

### 3.2.6 RGB composites delivered

The parameters can be combined between each other in RGB composites to highlight mineral associations or variations in the composition of the surface. **Table 1** shows examples of RGB composites used by previous authors, for the sake of clarity we arbitrary named the composites with consecutive numbers. Among them are the Clementine-like composite of Lucey et al. (2000), three composites suitable for the exploration of mafic minerals and evaluate surface maturity by Zambon et al. (2020) (RGB1, RGB2, and RGB3), two composites focused on crater ejecta by Horgan et al. (2014) (RGB4 and RGB5), two composites to detect mafic minerals by Besse et al. (2011) (RGB6 and RGB7), the olivine detection composite of Bretzfelder et al. (2020) (RGB8), and the spinel composite of Moriarty et al. (2022). Furthermore, other combinations of parameters can be done to highlight different compositions or mineral associations. For this reason, we created a python function that combines all the indexes in a single tiff file, this allows the user to reproduce each one of the listed RGB composites and more in a geoprocessing software like QGIS.

### 3.3 Deployment

**MoonIndex** is deployed as a python package with an MIT license. It is reachable from the web repositories PyPI and GitHub. Some exemplifying products will be showcased in the Space Browser of the EXPLORE platform (Nodjoumi et al., 2022). The

source code of the tool is fully available at GitHub (Suarez-Valencia, 2023), so the user has the option to modify it to its needs.

## 4 Results

In this section we will showcase our results obtained with the convex hull continuum-removal method for a selected set of indexes, that we will later compare with the results of previous authors. Nevertheless, the results for all the calculated indexes are reported in the supplementary materials (**Figure S4**). The analysis of the images and the subsequent interpretation of the mineralogy are particular to the selected study zones, so the user must consider the regional properties of their targets when using the products of *MoonIndex*.

### 4.1 Filtering

Our first goal was to reduce the noise of the data using a Fourier and a Gaussian filter without losing much scientific information of the general shape of the spectrum and the absorption bands. In **Figure 7c**, the ratio between the original image and the filtered one shows that the residual information is concordant with the stripes on the non-filtered cube (**Figure 7b**), furthermore, the crater in the bottom-left has little residuals, since the striping was not as strong in this location. Another test was to identify the pixels that overcame a change of over 2% during the filtering (**Figure 7d**), which are shown in black. These pixels are consistent with the original striping, which means that the surface information that was visible before the filtering (yellow) was not affected by the process.

### 4.2 Band center and depth

The bands centers and depths calculated by *MoonIndex* for the Apollo basin are shown in **Figure 9a, 9b, 9c, and 9d**. The band center defines the position of the absorption features to study, which in the case of pyroxenes and olivines is related to their composition (Burns, 1993; Klima et al. 2011). The band depth in turn reflects the amount of that mineral, since a stronger signal indicates a higher abundance within a mixture (Clouts et al., 1986). On the band center at 1  $\mu\text{m}$  there is a clear difference between the areas corresponding to highlands and maria (**Figure 9a**). The first ones have centering values around 0.93  $\mu\text{m}$ , indicating at least a lack of pyroxenes; while in the mare, the band is centered at longer wavelengths, around 1.04  $\mu\text{m}$ , resulting from the presence of pyroxene on the basaltic lavas (Klima et al., 2011). Furthermore, the variations inside the maria hints to a compositional variation of pyroxenes, since OPX tends to have lower center values than CPX. The band depth at 1  $\mu\text{m}$  also allows the identification of mafic minerals (**Figure 9c**), if the levels of space weathering is equivalent, greater band depths indicates a major abundance of them. The band depth at the center of the basin shows values around 0.13, while in the surrounding highlands it is only around 0.05. The position of the band center at 2  $\mu\text{m}$  inside the maria varies between 2.05 and 2.2  $\mu\text{m}$ , further pointing to some variations in the composition of pyroxenes. Finally, the band depth at 2  $\mu\text{m}$  shows strong absorption in the maria of around 0.08, further pointing to the presence of pyroxene (**Figure 9c and 9d**). Olivine does not show

features in the 2  $\mu\text{m}$  spectral range, so a comparison between both band depths can help identify its presence (see Index RGB 8) (Isaacson et al., 2011).

Some instrumental and acquisition artifacts are also seen. The band depth at 2  $\mu\text{m}$  is especially sensitive to the already mentioned thermal instrumental error that causes a decrease of the values from right to left of the  $M^3$  cubes at longer wavelengths (Green et al., 2011), resulting in the maria regions to the left of the image showing a similar depth as the highlands. Steep regions with high incidence angles show anomalous values on all the indexes, therefore information in those zones is not reliable.

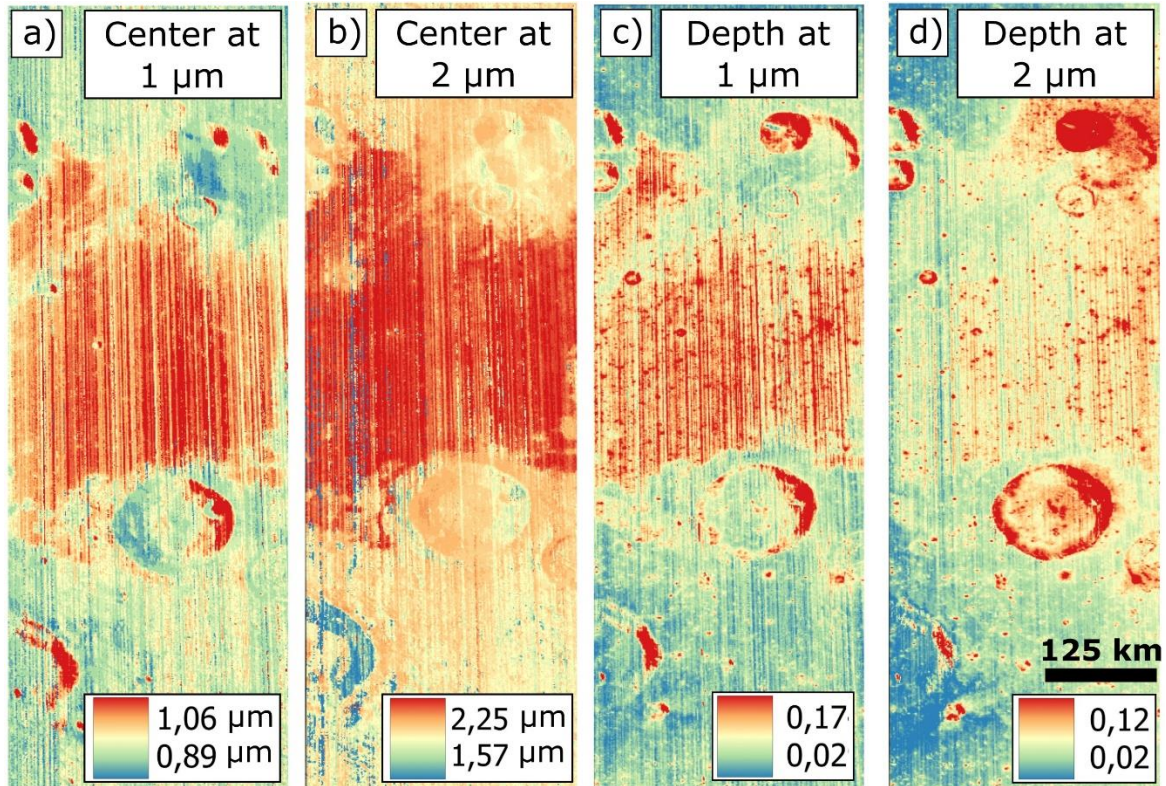


**Figure 9: Initial parameters calculated by *MoonIndex* for the Apollo basin. a) Band center at 1  $\mu\text{m}$ , lower values (blue) correspond to highlands materials, while higher values (red) are due to the presence of mafic minerals in the mare. b) Band depth at 2  $\mu\text{m}$ , also allows differentiation between highlands and mare. c y d) Band center and depth for 2  $\mu\text{m}$ , they serve a similar purpose as their 1  $\mu\text{m}$  counterparts.**

#### 4.3 Band area and asymmetry

To showcase the band area and asymmetry obtained by *MoonIndex*, we use the cubes over the Aristarchus crater, which has a well-preserved ejecta blanket around and a variety of glass-bearing materials (Mustard et al., 2011). The band area corresponds to the region inside the continuum and the absorption band (**Figure 2**). The band area is useful to identify ejecta (Horgan et al., 2014), as well as mineralogical differences, since OPX-rich ejecta has a higher band area value than CPX-rich ones (Cloutis et al., 1990).

The band asymmetry quantifies the shape of the absorption band by comparing the area to the left and right of the position of the band center, negative values imply a bigger area left of the center, and positive values the opposite. The band asymmetry is useful to identify glass and olivine-bearing ejecta, as well as plagioclase. Since mixtures of pyroxene with those materials result in higher asymmetries than only pyroxene (Horgan et al., 2014). For the band area at 1  $\mu\text{m}$  in the Aristarchus crater, the ejecta is clearly recognizable as a zone with low values scattered around the crater (**Figure 10a**). In the band asymmetry at 1  $\mu\text{m}$ , the only contrasting feature is the negative values of the northern ejecta (**Figure 10b**), which previous authors have identified as a mixture of OPX and anorthosite (Chevrel et al., 2009). In the band area at 2  $\mu\text{m}$ , the pattern of the ejecta is not so clear compared to its 1  $\mu\text{m}$  counterpart, the lower values in the southern half of the ejecta indicate a lower amount of pyroxene on it (**Figure 10c**). As for the band asymmetry at 2  $\mu\text{m}$  (**Figure 10d**), we found that the landforms are clearer than in its 1  $\mu\text{m}$  equivalent. Still, higher values are encountered in the ejecta south of the crater in both asymmetries, pointing to the presence of glass-bearing lithologies (Horgan et al., 2014).

Negative values dominate the 2  $\mu\text{m}$  asymmetry, meaning that the absorption band is broader left of the 2  $\mu\text{m}$  center. This effect is introduced by closing the absorption band

at 2.5  $\mu\text{m}$ , which cuts parts of the band at longer wavelengths and ends up affecting the area and shape of the band, and thus also the asymmetry.

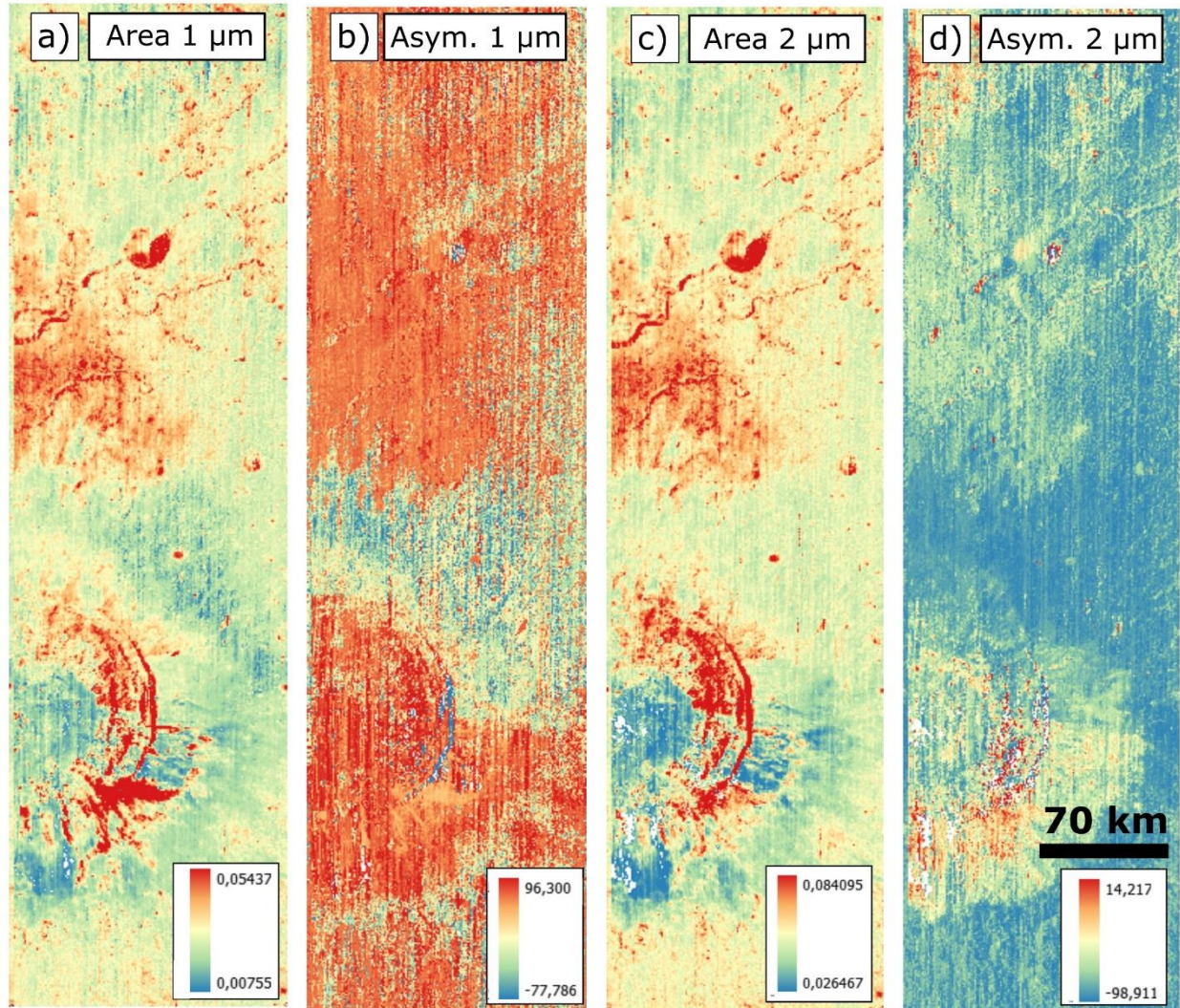


**Figure 10: Band areas and asymmetries calculated by *MoonIndex* for the Aristarchus crater. a) Band area at 1  $\mu\text{m}$ , the ejecta of the crater is clearly visible, the higher values, in red, indicate enrichment in OPX. b) Band asymmetry at 1  $\mu\text{m}$ , higher values indicate the existence of glass-bearing ejecta. c) Band area at 2  $\mu\text{m}$ , the low values at the southern part of the ejecta indicates low abundance of pyroxene. d) Band asymmetry at 2  $\mu\text{m}$ , higher values also point to glass-bearing ejecta, but the widespread lower values are due to the band being cut off at 2.5  $\mu\text{m}$ .**

#### 4.3 RGB composites

The Clementine-like color composite (Red: 750 nm/540 nm, Green: 750 nm/1000 nm, Blue: 540 nm/750 nm) produced by *MoonIndex* for the Vallis Alpes region is showcased in **Figures 11**. This composition, originally formulated by Lucey et al. (2000),

displays highlands material in red, due to glass agglutinates, and maria in yellow-green due to the combination of mafic minerals signals. Our result is concordant with this distribution, since the yellow location to the south of the image corresponds to the Imbrium mare, and the red zone that covers the majority of the image is the rim of the Imbrium basin, a highlands-like terrain. A smaller linear-shaped concentration of mafic minerals is also identifiable to the north, which is related to the basaltic flood inside the Vallis Alpes.

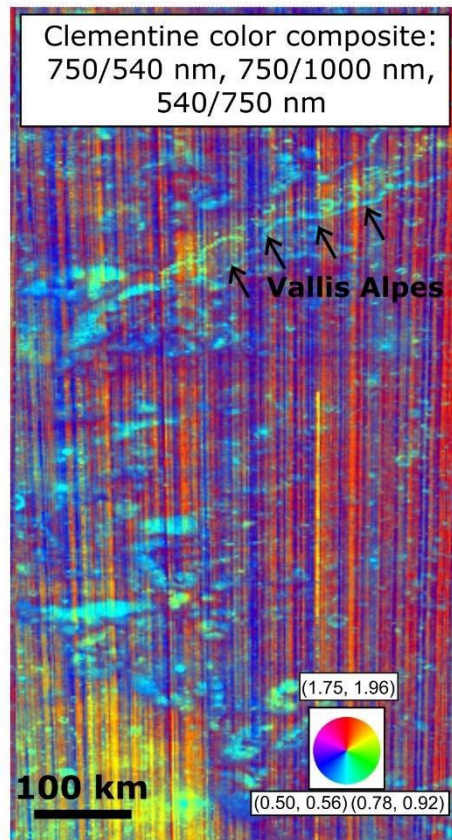


**Figure 11: Clementine-like color composite created with *MoonIndex*. The red channel is 750 nm/540 nm, the green channel is 750 nm/1000 nm, and the blue channel is 540 nm/750 nm. The highlands appear in red due to the concentration of glassy agglutinates, and the maria and basaltic floods appear in yellow-green due to the combination of mafic minerals. Vallis Alpes shows a signal pointing to mafic minerals.**

## 5 Discussion

### 5.1 Filtering

To evaluate the effect of the filters, we compared our results with the ones of Zambon et al. (2020) on the Apollo basin. **Figure 12** shows the position of the band centers at 1  $\mu\text{m}$ . A reduction in the number of vertical stripes is achieved with the combined filtering applied by *MoonIndex* (**Figure 12a**), this is more noticeable in the highlands around the Apollo basin, where the information of the surface is not so

distorted by vertical lines with anomalous values, as is the case for the band center of Zambon et al. (2020) (**Figure 12b**). Furthermore, the spectral patterns of the surface are maintained after the filtering, the higher values at the center of the basin and their progressive reduction to its edges is equally recorded in both images, meaning that details were not lost. This is also true for small surface features, like the several craters in the southern highlands (black circles in **Figure 12**), which can be recognized in both versions of the index by their centering at longer wavelengths compared to their surroundings. There are other filtering methods for hyperspectral data apart from the one used in this work, different approaches include the transformation of the data using Principal Component Analysis (PCA) combined with pixel local grounding (PLG) (Zhang et al. 2010), or some variation of the MNF method mentioned earlier (Luo et al., 2016). Further work is needed to test and implement these options in *MoonIndex*, which is facilitated and encouraged by the Open-Source nature of the tool. Another further implementation to enhance the visualization of the resulting indexes would be to remove pixels with high incidence angles, which would require the extraction of this metadata from the OBS.IMG file downloaded from the PDS and its integration to the code of *MoonIndex*.

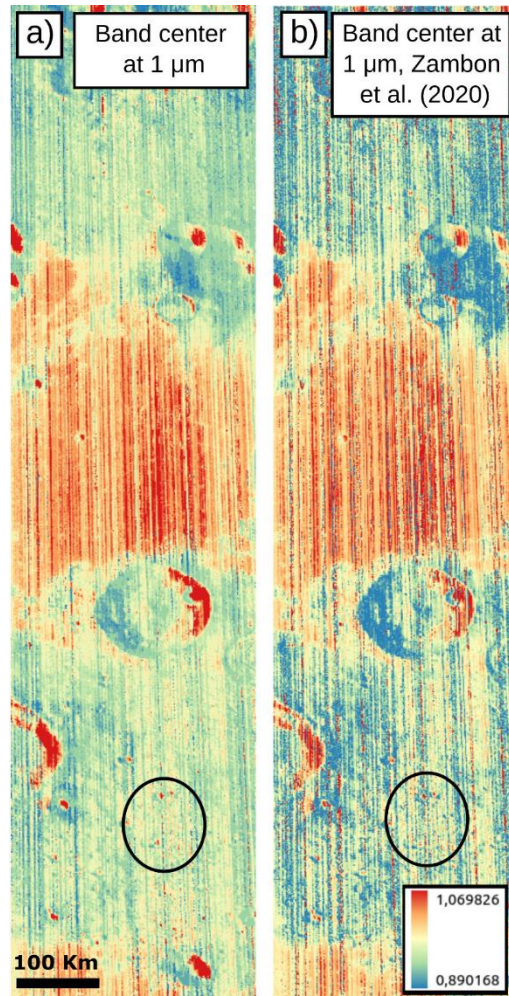


**Figure 12: Band centers at 1  $\mu\text{m}$  for the Apollo basin. a) Band center calculated in this work, after the Fourier and Gaussian filtering, the number of**

**vertical stripes is less than in a non-filtered cube, especially on the highlands. b) Band center calculated by Zambon et al. (2020). The black circles contain small craters, the signal of these geological features is maintained after the filtering, as well as the major spectral features.**

## 5.2 Parameters

The resemblance of our parameters with the ones in the literature varies. For the indexes that are formulated before the continuum removal, such as the Clementine-like index, the results are consistent with the original data, with changes only in the spatial resolution and the noise patterns, both particular to each instrument. Nevertheless, for the indexes obtained after the continuum removal, we identified variations with respect to the original formulations, which are related to the methodologies used by every author. In **Figure 13** we compare our results for the band center and depth at 1  $\mu\text{m}$  with the ones of Zambon et al. (2020). **Figure 13a** shows the ratio between the band centers, the major differences can be seen in red vertical lines and in the rims of big craters. The first ones are related to the removal of vertical stripes during the filtering, and the second ones to high incidence angles at the slopes of the craters. This indicates that there are no major variations in the surface data, except at particular locations inside big craters. The distribution of both histograms (this work in blue, Zambon et al. (2020) in red), also reflects a similar trend in both indexes (**Figure 13c**), most of the pixels in both cases are centered between 0.9 and 1.1  $\mu\text{m}$ . Still, the band centers of Zambon et al. (2020) have a slight shift to shorter wavelengths, especially in high-slope crater rims (**Figure 12b**). Major differences can be seen in the ratio of the band depth at 1  $\mu\text{m}$ . The red areas are widespread, and although most of them are due to the destripping of our data, changes are considerable in locations with clear signals of the surface (**Figure 13b**). This is more noticeable in the histograms of the band depths (**Figure 13d**), where the values of Zambon et al. (2020) accumulate more at higher values. As the band area and asymmetry are both derived and linked to the band depth, our results also diverge in a similar way from the ones of other authors. This major discrepancy in the band depth compared to the

band center is the result of using different continuum-removal methods, as we will discuss later.

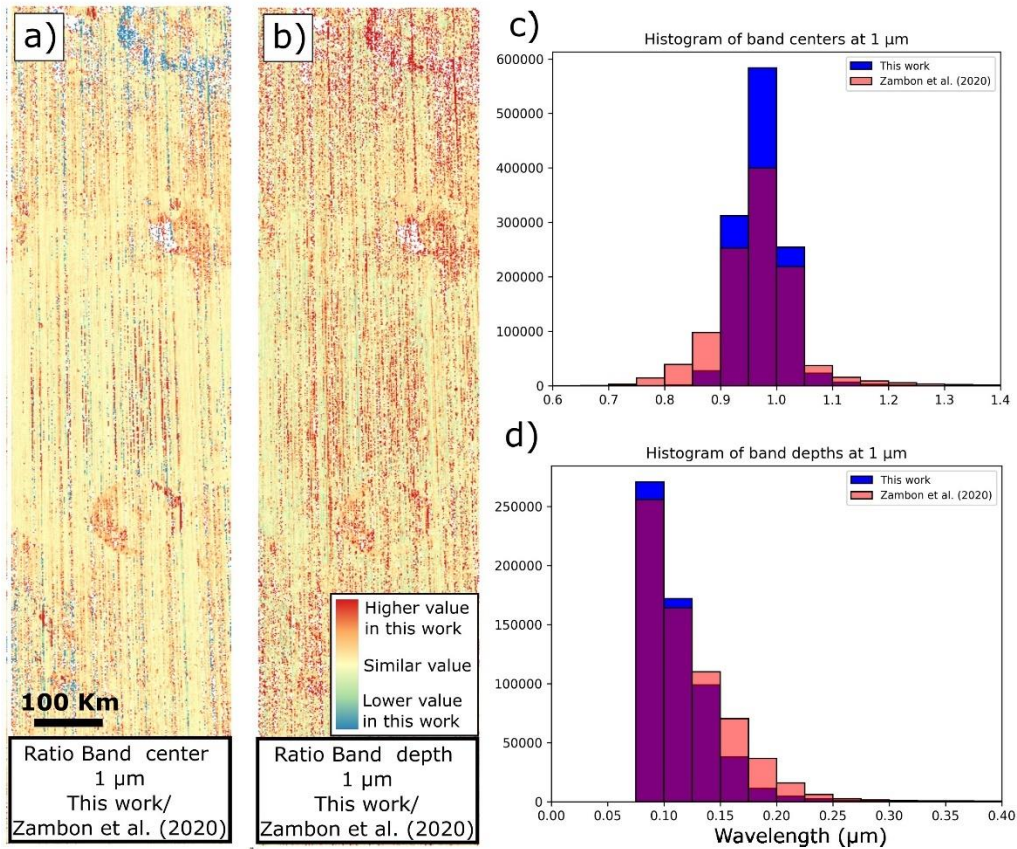


**Figure 13: Comparison of our results and the ones of Zambon et al. (2020), for the band center and depth at 1 μm in the Apollo Basin. a) Ratio of the band centers, the major differences correspond to removed noise or crater rims, b) Ratio of the band depths, more discrepancies can be seen apart of the stripes and crater rims, c) Histogram of values for the band centers, trends are similar, with a small shift to smaller wavelengths in Zambon et al. (2020), d) Histogram of values for the band depths, a bigger shift is seen in this case, as the results of Zambon et al. (2020) accumulates at higher values. The difference in the counts in the histogram is due to a major amount of no data pixels in the results of Zambon et al. (2020).**

#### 5.4 Color composite maps

The comparison of our RGB color composite maps with the ones in the literature presents certain difficulties. The source material from previous authors is not always available, therefore we cannot properly configure parameters like the band stretch or rendering method. Nevertheless, even when the specific colors and tonalities of the indexes may vary between works, the patterns of the geological features on the image and their differences should remain identifiable. This should allow for robust enough cartographic use of derived data.

The RGB 4 index (Red: Band center at 1  $\mu\text{m}$ , Green: Band center at 2  $\mu\text{m}$ , Blue: Band area at 1  $\mu\text{m}$ ) recreated in this work is close to the original one produced by Horgan et al. (2014) (**Figure 14a and 14b**) for the Aristarchus crater. The main colors are maintained, and the geological features are easily recognizable. This index is particularly useful to differentiate between pyroxenes, OPX is seen in blue, CPX in yellow, and a mix between them is green. Ejecta glass is also visible in magenta and orange. Although both indexes are generally compatible, there are some differences in the distribution. In our results the blue areas are smaller, indicating a lesser amount of OPX in the ejecta blanket. The black regions on the original index are pink in our work, which correspond to shadows or melt with no major signal around the 1  $\mu\text{m}$  band. On the other hand, the differences are bigger for the RGB 5 (Red: Band asymmetry at 1  $\mu\text{m}$ , Green: Band center at 1  $\mu\text{m}$ , blue: Band center at 2  $\mu\text{m}$ ), also originally formulated by Horgan et al. (2014) (**Figure 14c and 14d**). This index is intended to highlight glass-bearing lithologies due to their high asymmetries, which will appear in pink and yellow. Both indexes are consistent north of the Aristarchus crater; the large pink area north of the crater is followed by the yellow-dominated locations. To the south, the results of Horgan et al. (2014) show lesser amounts of glass, while ours have a pink area that fits well with the ejecta blanket of the crater. The index that differs the most with the one of Horgan et al. (2014) is the band asymmetry at 1  $\mu\text{m}$ , this is probably related to the continuum-removal method used by the prior authors, which applied a second order polynomial fit to the data.

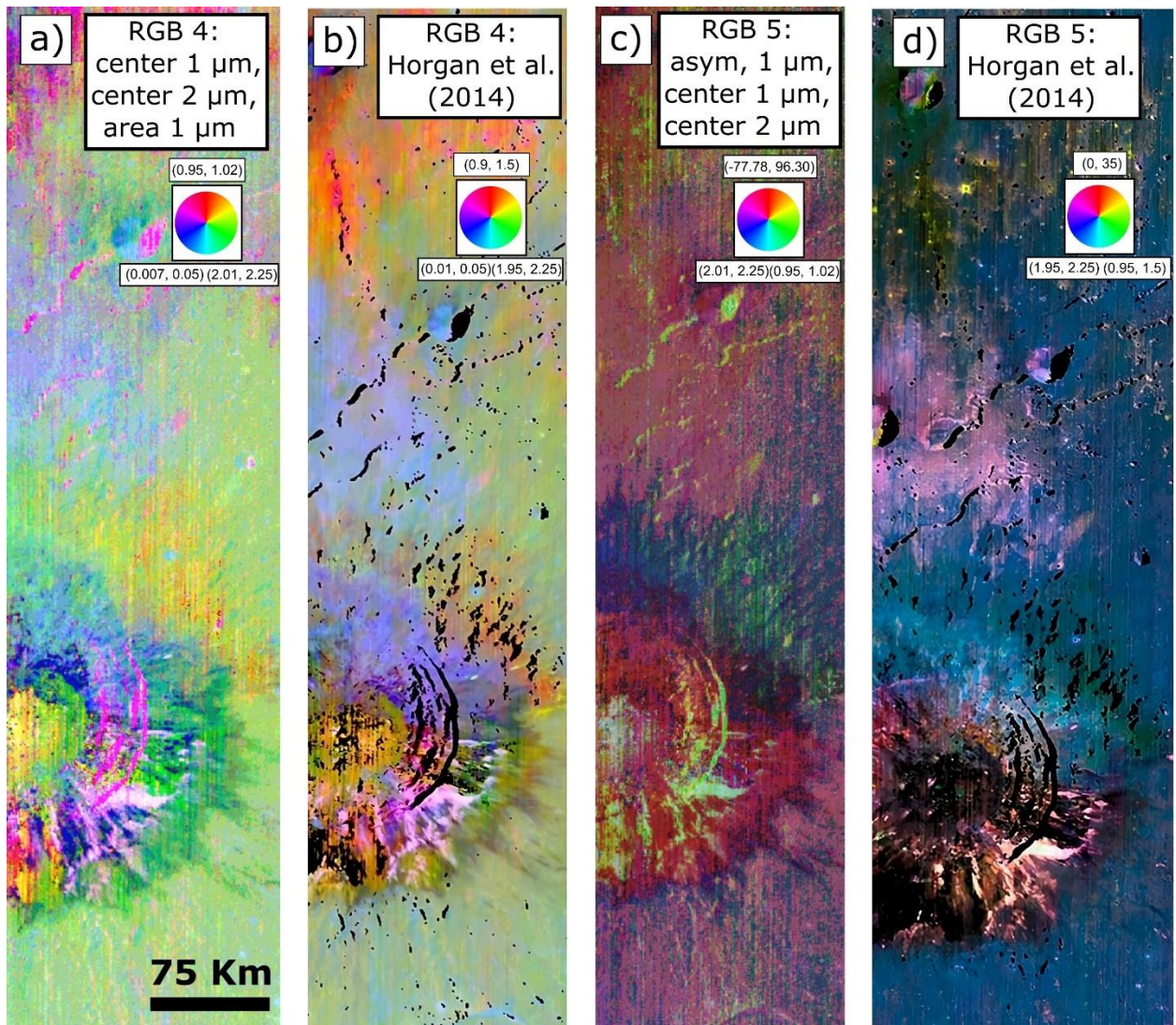


**Figure 14: Comparison between our results and the ones of Horgan et al. (2014) for the Aristarchus crater. a) RGB 4 recreated in this work, the red channel is the band center at 1  $\mu\text{m}$ , green is the band center 2  $\mu\text{m}$ , and blue is the band area at 1  $\mu\text{m}$ . b) original RGB 4 by Horgan et al. (2014), both color ramps are consistent, and the ejecta blanket and its compositional variation are seen in both cases, blue implies OPX, yellow CPX and green a mix of both. c) RGB 5 recreated in this work, the red channels are the band asymmetry at 1  $\mu\text{m}$ , green is the band center at 1  $\mu\text{m}$ , and blue is the band center at 2  $\mu\text{m}$ ; overlaid by the band area at 1  $\mu\text{m}$  in grayscale. d) original formulation of the RGB 5 by Horgan et al. (2014), the color ramp is less consistent, especially at the ejecta south of the crater, nevertheless the distribution of glass-bearing rocks (yellow and pink) is consistent north of the crater. The stretch values of Horgan et al. (2014) are unknown.**

Another index worth comparing is RGB 8 (Red: Band depth at 1.9  $\mu\text{m}$ , Green: IBD at 2  $\mu\text{m}$ , Blue: IBD at 1  $\mu\text{m}$ ), originally formulated by Bretzfelder et al. (2020) for the Vallis Alpes region. On the original index, yellow corresponds to OPX, cyan to CPX,

and most important, dark blue shows olivine-bearing massifs. Our results show a different color ramp (**Figure 15**). This occurs because we used a modified method to calculate the band depth at 1.9  $\mu\text{m}$ ; instead of creating a specific continuum for the band, we measure the depth directly on the convex-hull removed spectra. But even if the calculation and the resulting color ramp are different, the same geological patterns are still identifiable in both composites. In our results, CPX is still yellow, OPX is light-toned blue, and olivine-bearing rocks appear in dark purple. An example of the last is the isolated mountain next to the southern edge of Vallis Alpes, which shows a strong olivine signal in both indexes (**Figure 15**). Since this index was thought specifically to identify olivine, our result is still relevant and applicable for that purpose.

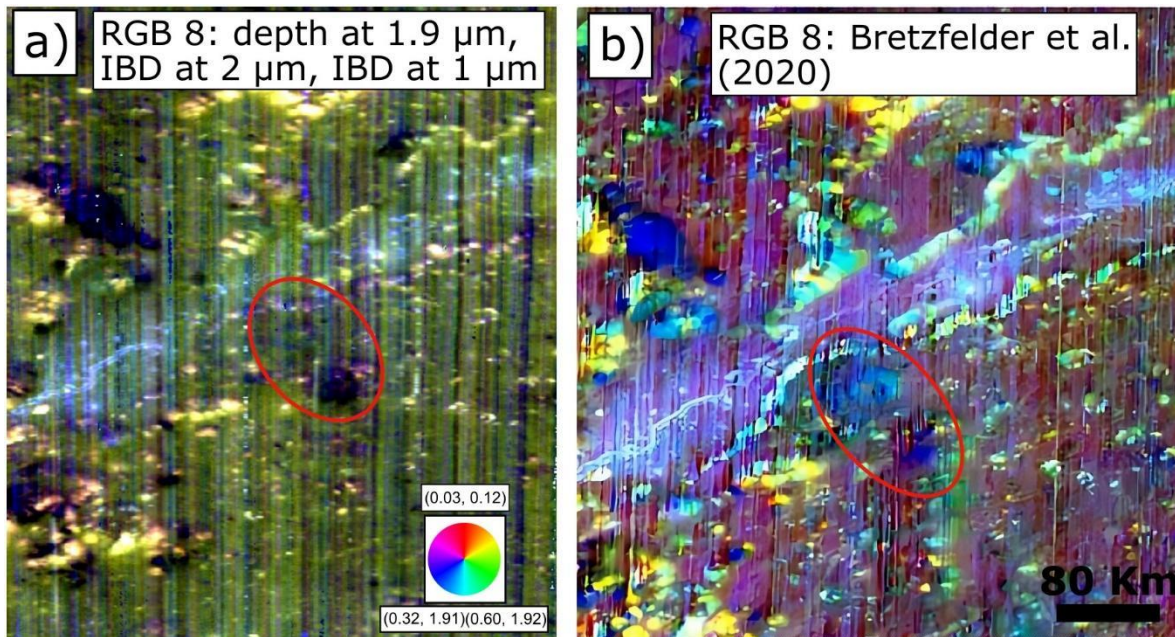


**Figure 15: Comparison between our results and the ones of Bretzfelder et al. (2020) for the Vallis Alpes. a) RGB 8 recreated in this work, red is the band depth at 1.9  $\mu\text{m}$ , green is IBD at 2  $\mu\text{m}$ , and blue is IBD at 1  $\mu\text{m}$ . b) original formulation of the RGB 8 by Bretzfelder et al. (2020). Stretch values are unknown. The ramp color is different in both cases, due to a change in the calculation of the band depth at 1.9  $\mu\text{m}$ . Nevertheless, the pattern of geological features is maintained, for example the dark blue spots on the original index correspond to olivine (red circle), and in our recreation those same areas appear purple.**

### 5.5 Effect of the continuum-removal method

The differences between our results and the ones of the previous authors are produced by several factors. The method used to remove the continuum is the main variable affecting the indexes. Since most of the previous authors used a combination of linear fits and second-order fits within defined intervals (Horgan et al., 2014, Zambon et al., 2020), a comparison between the results of our convex hull and second-and-first-order fit methods is helpful to explain the changes.

The general shape of the resulting continuum-removed spectrum is similar in both methods (**Figure 16a**), and all the parameters of the absorption bands are well represented and easily measurable. The position of the band center is not greatly affected by the removal method; the average difference between both procedures is 5 nm at the 1  $\mu\text{m}$  absorption band, and 25 nm at the 2  $\mu\text{m}$  band, which is in both cases smaller than the spectral sampling of  $M^3$  for those regions. On the other hand, the band depth is especially sensitive to the selected method, which can be appreciated by subtracting the images (**Figure 16b**). At 1  $\mu\text{m}$  the band depth varies considerably, higher values are obtained with the second-and-first-order fit method in the highlands (**Figure 16a**), while in the mare the result is the opposite (**Figure 16c**). This inconsistency is the result of the way in which both methods define the continuum line. The second-and-first-order fit interpolates a second order polynomial function between two arbitrarily defined shoulders, while the convex hull draws a straight line connecting the local maximums it automatically computes (**Figure 8**). Hence, when the absorption band is weak, like on the highlands, the concave shape of the second-and-first-order fit method creates a slightly higher distance to the spectrum, resulting in bigger band depth values (**Figure 16d**). As for the maria regions, it looks like the convex hull method is identifying the right shoulder at longer wavelengths, which produces a deeper band depth. The band depth at 2  $\mu\text{m}$  is less affected by the method, the variation is lower than in the 1  $\mu\text{m}$  band, and most of the values are inside one standard deviation (**Figure 16e**). The second-and-first-order fit method uses a straight line for the 2  $\mu\text{m}$  absorption band, thus the result is closer to the also linear interpolation done by the convex hull. Subsequent indexes like the band area and asymmetry are also affected in similar ways, especially at the 1  $\mu\text{m}$  absorption bands, as larger band depths will result in larger band areas.

Several other factors are surely responsible for changes on the resulting indexes, but the lack of source materials for some of the indexes makes them difficult to evaluate. During the preprocessing of the data many factors could change, if the authors applied custom filtering or workflows before calculating the indexes, that would affect the end-result. Another difficulty is added to the RGB composites, even if the formulations are similar, we cannot be sure of the color stretch or the display settings of the original indexes. Small changes in the intervals of the values displayed by each channel can greatly modify the color ramp of a composite. In any case, the geological and spectral features on our composites are consistent with the original ones regardless of their tonality, so the products of *MoonIndex* appear to be reliable for geological analysis.

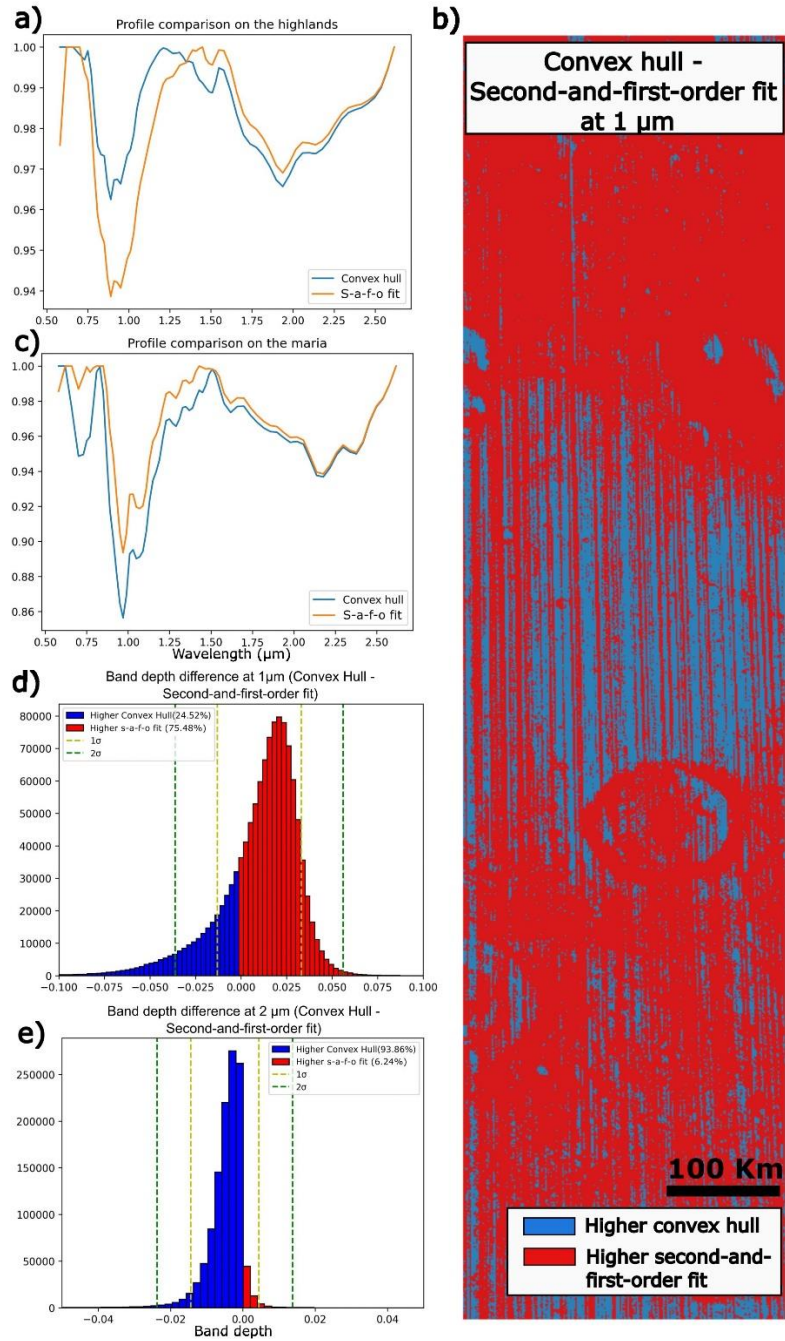


**Figure 16: Comparison between the band depth results of the convex hull and the second-and-first-order fit methods for the Apollo basin. a) Spectral profiles of the same pixel on the highlands using the two methods, the band depth is greater with the second-and-first-order fit method. b) Image showing the difference between the results of the methods, in red regions where the second-and-first-order fit returned higher values, in blue the opposite. c) Spectral profiles on the mare, this time the convex hull has a higher band depth. d) Histogram of the values at 1 μm, the values are scattered more than two standard deviations. e) Histogram of the**

**values at 2  $\mu\text{m}$ , the difference between both methods is close to zero, and the values are not so scattered.**

The reconstruction of spectral indexes from such varied sources makes it difficult to accomplish a high fidelity in all of them. This is especially true when some of those indexes were formulated several years ago, with different missions, methodologies, and technologies. Nevertheless, our methodologies and results are consistent with each other, so the analyses derived from them are complementary and comparable. Given this context, consistency between the data is important when applied to the geological analysis of a region on the Moon, so we recommend the users of *MoonIndex* to use only one of the continuum removal methods for each project they might work on.

## 6 Conclusions

Spectral indexes are an easy and versatile way to approach the compositional analysis of the Moon. **Table 1** highlights proven indexes found in the literature, but other operations or RGB composites can be made with the products of *MoonIndex* to explore different mineralogical properties. During our recreation of the spectral indexes in python we added certain improvements to the data of  $M^3$ . The Gaussian and Fourier filtering proved useful to reduce the vertical striping typical of  $M^3$  cubes, allowing the retrieval of clearer spectra, especially from cubes that otherwise would be almost useless for geological interpretation.

The implementation of the convex hull method to remove the continuum has certain advantages over the second-and-first-order fit method. As it creates an envelope over the local maximums, the shape of the absorption bands present on the spectrum should be identified correctly. Furthermore, the convex hull works automatically over the data, removing the necessity of establishing arbitrary limits for the interpolations. We recommend the use of the convex hull method over the second-and-first-order fit method, still both methods are implemented in *MoonIndex*.

The fidelity of the reconstructed indexes varies for several reasons. The most important one is related to the use of the convex hull method to remove the continuum, opposite to the polynomial fits applied by previous authors. But other factors unreported in the literature likely affected the results, such as the preprocessing routines, filtering methods, or the visualization parameters of the composites. Nevertheless, despite some changes in tonalities and values, the reproduced indexes have a similar scientific meaning in all cases and highlight the same compositional properties as the original formulations. The indexes produced by *MoonIndex* are consistent with each other, but the methodologies and algorithms described in this work should be considered when comparing them with indexes from other works.

Finally, *MoonIndex* was created to give a better accessibility to this kind of products to the scientific community. The package is Open-Source and freely available, so the users can modify it for their own purposes. The necessity to preprocess the data in other not-so-intuitive software like ISIS and GDAL may make the task difficult, but other tools like the EXPLORE platform or the GMAP Jupyter Hub (Nodjoumi et al., 2022), could contribute to ease the process. It is worth mentioning that the commercial software ENVI is typically used instead of ISIS for georeferencing and calibrating  $M^3$  data, and

although we advocate for freely accessible software, the products derived from ENVI could be processed by *MoonIndex* without problems after being ingested to Python.

## Acknowledgments

This research was done on the framework of the EXPLORE project, that has received funding from the European Union's 2020 research and innovation program under grant agreement No 101004214. Additionally, we had support from the GMAP project, part of the Europlanet 2024 RI has received funding from the European Union's Horizon 2020 research and innovation programme under grant agreement No 871149.

## Open Research

*MoonIndex* is available for Python 3.10 and higher in the PyPI repository. The tool is released under the GNU general public license. The source code, exemplary Jupyter notebooks, definition of functions, and workflows can be accessed via GitHub and Zenodo (Suarez-Valencia, 2024). The raw datasets used in this work can be accessed through the PDS, and versions ready to use on *MoonIndex* are reachable at: Suarez-Valencia et al. (2024).

## References

- Acton, C., Bachman, N., Semenov, B., & Wright, E. (2016). SPICE TOOLS SUPPORTING PLANETARY REMOTE SENSING. *The International Archives of the Photogrammetry, Remote Sensing and Spatial Information Sciences, XLI-B4*, 357-359. <https://doi.org/10.5194/isprs-archives-XLI-B4-357-2016>
- Adams, J. B. (1974). Visible and near-infrared diffuse reflectance spectra of pyroxenes as applied to remote sensing of solid objects in the solar system. *Journal of Geophysical Research*, 79(32), 4829–4836. <https://doi.org/10.1029/jb079i032p04829>
- Adams, J. B. & Filice, A. L. (1967). Spectral reflectance 0.4 to 2.0 microns of silicate rock powders. *Journal of Geophysical Research*, 72(22), 5705–5715. <https://doi.org/10.1029/jz072i022p05705>
- Adams, J. B. & McCord, T. B. (1971). Alteration of Lunar Optical Properties: Age and composition effects. *Science*, 171 (3971), 567–571. <https://doi.org/10.1126/science.171.3971.567>
- Adams, J. B., Smith, M. O., Gillespie, A. R., Pieters, C. M., & Englert, P. A. J. (1993). Remote geochemical analysis: Elemental and mineralogical composition. *Imaging spectroscopy: Interpretation based on spectral mixture analysis*, 145-166.

- Agrell, S. O., Scoon, J. H., Muir, I. D., Long, J. V. P., McConnell, J. D., & Peckett, A. (1970). Observations on the chemistry, mineralogy and petrology of some Apollo 11 lunar samples. *Geochimica et Cosmochimica Acta Supplement*, 1, 93.
- Albee, A. L. (2003). Lunar Rocks. In Elsevier eBooks (S. 825–837). <https://doi.org/10.1016/b0-12-227410-5/00390-2>
- Arnold, J. A., Glotch, T. D., Lucey, P. G., Song, E., Thomas, I. R., Bowles, N. E., & Greenhagen, B. T. (2016). Constraints on olivine-rich rock types on the Moon as observed by Diviner and M<sup>3</sup>: Implications for the formation of the lunar crust: CONSTRAINTS ON OLIVINE-RICH ROCK TYPES ON THE MOON. *Journal of Geophysical Research: Planets*, 121(7), 1342-1361. <https://doi.org/10.1002/2015JE004874>
- Bandfield, J. L., Poston, M. J., Klima, R. L., & Edwards, C. S. (2018). Widespread distribution of OH/H<sub>2</sub>O on the lunar surface inferred from spectral data. *Nature Geoscience*, 11(3), 173-177. <https://doi.org/10.1038/s41561-018-0065-0>
- Besse, S., Sunshine, J. M., Staid, M. I., Petro, N. E., Boardman, J. W., Green, R. O., Head, J. W., Isaacson, P. J., Mustard, J. F., & Pieters, C. M. (2011). Compositional variability of the Marius Hills volcanic complex from the Moon Mineralogy Mapper (M<sup>3</sup>). *Journal of Geophysical Research*, 116, E00G13. <https://doi.org/10.1029/2010JE003725>
- Bradski, G. (2000). The OpenCV Library. *Dr. Dobb's Journal of Software Tools*.
- Bretzfelder, J. M., Klima, R. L., Greenhagen, B. T., Buczkowski, D. L., Petro, N. E., & Day, M. (2020). Identification of Potential Mantle Rocks Around the Lunar Imbrium Basin. *Geophysical Research Letters*, 47(22). <https://doi.org/10.1029/2020GL090334>
- Burns, R. G. (1993). Mineralogical applications of Crystal field Theory. <https://doi.org/10.1017/cbo9780511524899>
- Cheek, L. C., Hanna, K. L. D., Pieters, C. M., Head, J. W. & Whitten, J. L. (2013). The distribution and purity of anorthosite across the Orientale Basin: New perspectives from Moon Mineralogy Mapper Data. *Journal of Geophysical Research: Planets*, 118(9), 1805–1820. <https://doi.org/10.1002/jgre.20126>

- Chevrel, S., Pinet, P., Daydou, Y., Mouëlic, S.L., Langevin, Y., Costard, F. & Erard, S. (2009). The Aristarchus plateau on the Moon: Mineralogical and structural study from Integrated Clementine UV–VIS–NIR Spectral data. *Icarus*, 199 (1), 9–24. <https://doi.org/10.1016/j.icarus.2008.08.005>
- Clark, R. N. & Roush, T. L. (1984c). Reflectance Spectroscopy: quantitative analysis techniques for remote sensing applications. *Journal of Geophysical Research*, 89(B7), 6329–6340.  
<https://doi.org/10.1029/jb089ib07p06329>
- Clark, R. N., Pieters, C. M., Green, R. O., Boardman, J. W., & Petro, N. E. (2011). Thermal removal from near-infrared imaging spectroscopy data of the Moon. *Journal of Geophysical Research*, 116, E00G16. <https://doi.org/10.1029/2010JE003751>
- Clenet, H. (2009). *Téledétection hyperspectrale: Minéralogie et pétrologie, Application au volcan Syrtis Major (Mars) et à l'ophiolite d'Oman*. Université de Toulouse.
- Cloutis, E. A., Gaffey, M. J., Jackowski, T. L. & Reed, K. L. (1986). Calibrations of phase abundance, composition, and particle size distribution for olivine-orthopyroxene mixtures from reflectance spectra. *Journal of Geophysical Research*, 91(B11), 11641. <https://doi.org/10.1029/jb091ib11p11641>
- Cloutis, E. A., Gaffey, M. J., Smith, D. G. & St J Lambert, R. (1990). Reflectance spectra of glass-bearing mafic silicate mixtures and spectral deconvolution procedures. *Icarus*, 86(2), 383–401.  
[https://doi.org/10.1016/0019-1035\(90\)90226-y](https://doi.org/10.1016/0019-1035(90)90226-y)
- Cloutis, E. A., Sunshine, J. M., & Morris, R. V. (2004). Spectral reflectance-compositional properties of spinels and chromites: Implications for planetary remote sensing and geothermometry. *Meteoritics & Planetary Science*, 39(4), 545-565. <https://doi.org/10.1111/j.1945-5100.2004.tb00918.x>
- Corley, L. M., McGovern, P. J., Kramer, G. Y., Lemelin, M., Trang, D., Gillis-Davis, J. J., Taylor, G. J., Powell, K. E., Kiefer, W. S., Wieczorek, M., & Zuber, M. T. (2018). Olivine-bearing lithologies on the Moon: Constraints on origins and transport mechanisms from M3 spectroscopy, radiative transfer modeling, and GRAIL crustal thickness. *Icarus*, 300, 287-304.  
<https://doi.org/10.1016/j.icarus.2017.09.012>
- Farrand, W. H., Bell, J. F., Johnson, J. R., Squyres, S. W., Soderblom, J., & Ming, D. W. (2006). Spectral variability among rocks in visible and near-infrared multispectral Pancam data collected at Gusev

- crater: Examinations using spectral mixture analysis and related techniques. *Journal of Geophysical Research: Planets*, 111(E2), 2005JE002495. <https://doi.org/10.1029/2005JE002495>
- Figuera, R. M., Huu, B. P., Rossi, A. P., Minin, M., Flahaut, J. & Halder, A. (2018). Online characterization of planetary surfaces: PlanetServer, an open-source analysis and visualization tool. *Planetary and Space Science*, 150, 141–156. <https://doi.org/10.1016/j.pss.2017.09.007>
- Gillies, S. & others. (2013). *Rasterio: Geospatial raster I/O for Python programmers*. Mapbox. <https://github.com/mapbox/rasterio>
- Graham, R. L. (1972). An efficient algorithm for determining the convex hull of a finite planar set. *Information Processing Letters*, 1(4), 132-133. [https://doi.org/10.1016/0020-0190\(72\)90045-2](https://doi.org/10.1016/0020-0190(72)90045-2)
- Green, R. O., Pieters, C., Mouroulis, P., Eastwood, M., Boardman, J., Glavich, T., Isaacson, P., Annadurai, M., Besse, S., Barr, D., Buratti, B., Cate, D., Chatterjee, A., Clark, R., Cheek, L., Combe, J., Dhingra, D., Essandoh, V., Geier, S., ... Wilson, D. (2011). The Moon Mineralogy Mapper (M<sup>3</sup>) imaging spectrometer for lunar science: Instrument description, calibration, on-orbit measurements, science data calibration and on-orbit validation. *Journal of Geophysical Research*, 116, E00G19. <https://doi.org/10.1029/2011JE003797>
- Hapke, B. (1993). *Theory of Reflectance and Emittance Spectroscopy* (1.<sup>a</sup> ed.). Cambridge University Press. <https://doi.org/10.1017/CBO9780511524998>
- Hapke, B. (2001). Space weathering from Mercury to the asteroid Belt. *Journal of Geophysical Research*, 106(E5), 10039–10073. <https://doi.org/10.1029/2000je001338>
- Harris, C. R., Millman, K. J., Van Der Walt, S. J., Gommers, R., Virtanen, P., Cournapeau, D., Wieser, E., Taylor, J., Berg, S., Smith, N. J., Kern, R., Picus, M., Hoyer, S., Van Kerkwijk, M. H., Brett, M., Haldane, A., Del Río, J. F., Wiebe, M., Peterson, P., ... Oliphant, T. E. (2020). Array programming with NumPy. *Nature*, 585(7825), 357-362. <https://doi.org/10.1038/s41586-020-2649-2>
- Hazen, R. M., Mao, H. K. & Bell, P. M. (1978). Effects of compositional variation on absorption spectra of lunar pyroxenes. *Lunar and Planetary Science Conference Proceedings*, 1, 1081–1090. <https://ntrs.nasa.gov/search.jsp?R=19780057713>
- Hiesinger, H. & Head, J. W. (2006). New Views of Lunar Geoscience: An Introduction and Overview. *Reviews in mineralogy and geochemistry*, 60(1), 1–81. <https://doi.org/10.2138/rmg.2006.60.1>

- Horgan, B. H. N., Cloutis, E. A., Mann, P., & Bell, J. F. (2014). Near-infrared spectra of ferrous mineral mixtures and methods for their identification in planetary surface spectra. *Icarus*, 234, 132-154. <https://doi.org/10.1016/j.icarus.2014.02.031>
- Hoyer, S., & Joseph, H. (2017). xarray: N-D labeled Arrays and Datasets in Python. *Journal of Open Research Software*, 5(1). <https://doi.org/10.5334/jors.148>
- Hunter, J. D. (2007). Matplotlib: A 2D Graphics Environment. *Computing in Science & Engineering*, 9(3), 90-95. <https://doi.org/10.1109/MCSE.2007.55>
- Ivanov, M. A., Hiesinger, H., Van Der Bogert, C. H., Orgel, C., Pasckert, J. H., & Head, J. W. (2018). Geologic History of the Northern Portion of the South Pole-Aitken Basin on the Moon. *Journal of Geophysical Research: Planets*, 123(10), 2585-2612. <https://doi.org/10.1029/2018JE005590>
- Isaacson, P., Pieters, C. M., Besse, S., Clark, R. N., Head, J. W., Klima, R. L., Mustard, J. F., Petro, N. E., Staid, M., Sunshine, J. M., Taylor, L. A., Thaisen, K. G. & Tompkins, S. (2011). Remote Compositional Analysis of Lunar Olivine-rich Lithologies with Moon Mineralogy Mapper (M<sup>3</sup>) Spectra. *Journal of Geophysical Research*, 116. <https://doi.org/10.1029/2010je003731>
- Karr, C. (1975). Infrared and Raman spectroscopy of lunar and terrestrial minerals. In *Elsevier eBooks*. <https://doi.org/10.1016/c2013-0-10938-5>
- King, T. V. V., & Ridley, W. I. (1987). Relation of the spectroscopic reflectance of olivine to mineral chemistry and some remote sensing implications. *Journal of Geophysical Research: Solid Earth*, 92(B11), 11457-11469. <https://doi.org/10.1029/JB092iB11p11457>
- Klima, R. L., Pieters, C. M., Boardman, J. W., Green, R. O., Head, J. W., Isaacson, P. J., Mustard, J. F., Nettles, J. W., Petro, N. E., Staid, M. I., Sunshine, J. M., Taylor, L. A., & Tompkins, S. (2011). New insights into lunar petrology: Distribution and composition of prominent low-Ca pyroxene exposures as observed by the Moon Mineralogy Mapper (M<sup>3</sup>). *Journal of Geophysical Research*, 116, E00G06. <https://doi.org/10.1029/2010JE003719>
- Klima, R. L., Pieters, C. M., & Dyar, M. D. (2007). Spectroscopy of synthetic Mg-Fe pyroxenes I: Spin-allowed and spin-forbidden crystal field bands in the visible and near-infrared. *Meteoritics & Planetary Science*, 42(2), 235-253. <https://doi.org/10.1111/j.1945-5100.2007.tb00230.x>

- Klima, R. L., Dyar, M. D. & Pieters, C. M. (2011). Near-infrared spectra of clinopyroxenes: effects of calcium content and crystal structure. *Meteoritics & Planetary Science*, 46(3), 379–395.  
<https://doi.org/10.1111/j.1945-5100.2010.01158.x>
- Kodikara, G. R. L., Champati Ray, P. K., Chauhan, P., & Chatterjee, R. S. (2016). Spectral mapping of morphological features on the moon with MGM and SAM. *International Journal of Applied Earth Observation and Geoinformation*, 44, 31-41. <https://doi.org/10.1016/j.jag.2015.07.003>
- Laura, J., Acosta, A., Addair, T., Adoram-Kershner, L., Alexander, J., Alexandrov, O., Alley, S., Anderson, D., Anderson, J., Anderson, J., Annex, A., Archinal, B., Austin, C., Backer, J., Barrett, J., Bauck, K., Bauers, J., Becker, K., Becker, T., ... Young, A. (2023). *Integrated Software for Imagers and Spectrometers (7.2.0\_RC1)* [Software]. Zenodo. <https://doi.org/10.5281/ZENODO.2563341>
- Lawrence, D. J., Feldman, W. C., Barraclough, B. L., Binder, A. B., Elphic, R. C., Maurice, S., & Thomsen, D. R. (1998). Global Elemental Maps of the Moon: The Lunar Prospector Gamma-Ray Spectrometer. *Science*, 281(5382), 1484-1489. <https://doi.org/10.1126/science.281.5382.1484>
- Li, S., & Milliken, R. E. (2016). An empirical thermal correction model for Moon Mineralogy Mapper data constrained by laboratory spectra and Diviner temperatures. *Journal of Geophysical Research: Planets*, 121(10), 2081-2107. <https://doi.org/10.1002/2016JE005035>
- Liu, J. G., & Mason, P. J. (2009). *Essential Image Processing and GIS for Remote Sensing* (1.<sup>a</sup> ed.). Wiley.  
<https://doi.org/10.1002/9781118687963>
- Lucey, P. G., Blewett, D. T., & Jolliff, B. L. (2000). Lunar iron and titanium abundance algorithms based on final processing of Clementine ultraviolet-visible images. *Journal of Geophysical Research: Planets*, 105(E8), 20297-20305. <https://doi.org/10.1029/1999JE001117>
- Lucey, P. G., Blewett, D. T., Taylor, G. J., & Hawke, B. R. (2000). Imaging of lunar surface maturity. *Journal of Geophysical Research: Planets*, 105(E8), 20377-20386.  
<https://doi.org/10.1029/1999JE001110>
- Lucey, P. G., Greenhagen, B., Donaldson Hanna, K., Bowles, N., Flom, A., & Paige, D. A. (2021). Christiansen Feature Map From the Lunar Reconnaissance Orbiter Diviner Lunar Radiometer Experiment: Improved Corrections and Derived Mineralogy. *Journal of Geophysical Research: Planets*, 126(6). <https://doi.org/10.1029/2020JE006777>

- Lundeen, S., McLaughlin, S., & Alanis, R. (2011). *Moon Mineralogy Mapper Data Product Software Interface Specification* (39032; p. 111). JPL.
- Luo, G., Chen, G., Tian, L., Qin, K., & Qian, S.-E. (2016). Minimum Noise Fraction versus Principal Component Analysis as a Preprocessing Step for Hyperspectral Imagery Denoising. *Canadian Journal of Remote Sensing*, 42(2), 106-116. <https://doi.org/10.1080/07038992.2016.1160772>
- Malaret, E., P. Guasqui, S. McLaughlin, J. Sunshine, S. Besse, R. Clark, and P. Isaacson, CH1-ORB MOON M3 4 L2 REFLECTANCE NEAR-IR SPECTRAL IMAGES V1.0, CH1-ORB-L-M3-4-L2-REFLECTANCE-V1.0, NASA Planetary Data System, 2011. <https://doi.org/10.17189/1520414>
- McCord, T. B., Charette, M. P., Johnson, T. V., Lebofsky, L. A., Pieters, C., & Adams, J. B. (1972). Lunar spectral types. *Journal of Geophysical Research*, 77(8), 1349-1359. <https://doi.org/10.1029/JB077i008p01349>
- Montero, D., Aybar, C., Mahecha, M. D., Martinuzzi, F., Söchting, M., & Wieneke, S. (2023). A standardized catalogue of spectral indices to advance the use of remote sensing in Earth system research. *Scientific Data*, 10(1), 197. <https://doi.org/10.1038/s41597-023-02096-0>
- Moriarty, D. P., Simon, S. B., Shearer, C. K., Haggerty, S. E., Petro, N., & Li, S. (2023). Orbital Characterization of the Composition and Distribution of Spinel Across the Crisium Region: Insight From Luna 20 Samples. *Journal of Geophysical Research: Planets*, 128(5), e2022JE007482. <https://doi.org/10.1029/2022JE007482>
- Mustard, J. F., Pieters, C. M., Isaacson, P. J., Head, J. W., Besse, S., Clark, R. N., Klima, R. L., Petro, N. E., Staid, M. I., Sunshine, J. M., Runyon, C. J., & Tompkins, S. (2011). Compositional diversity and geologic insights of the Aristarchus crater from Moon Mineralogy Mapper data. *Journal of Geophysical Research*, 116, E00G12. <https://doi.org/10.1029/2010JE003726>
- Nodjoumi, G., Brandt, C., & Rossi, A. P. (2022, junio). *OPEN-SOURCE PLANETARY DATA PROCESSING ENVIRONMENTS BASED ON JUPYTERHUB AND DOCKER CONTAINERS*.
- Nozette, S. (1995). The Clementine mission: Past, present, and future. *Acta Astronautica*, 35, 161-169. [https://doi.org/10.1016/0094-5765\(94\)00181-K](https://doi.org/10.1016/0094-5765(94)00181-K)

- Moriarty, D. P., & Pieters, C. M. (2018). The character of South Pole-Aitken Basin: Patterns of surface and subsurface composition. *Journal of Geophysical Research: Planets*, 123(3), 729-747.  
<https://doi.org/10.1002/2017je005364>
- Ohtake, M., Matsunaga, T., Haruyama, J., Yokota, Y., Morota, T., Honda, C., Ogawa, Y., Torii, M., Miyamoto, H., Arai, T., Hirata, N., Iwasaki, A., Nakamura, R., Hiroi, T., Sugihara, T., Takeda, H., Otake, H., Pieters, C. M., Saiki, K., . . . Josset, J. (2009). The global distribution of pure anorthosite on the moon. *Nature*, 461(7261), 236–240. <https://doi.org/10.1038/nature08317>
- Pieters, C. M., Boardman, J., Buratti, B., Chatterj, A., Clark, R., Glavich, T., Green, R., Malaret, E., McCord, T., Mustard, J., Petro, N., Runyon, C., Staid, M., Sunshine, J., Tay, L., Tompkins, S., Varanasi, P., & White, M. (2009). *The Moon Mineralogy Mapper (M<sup>3</sup>) on Chandrayaan-1*.
- Pieters, C. M., Goswami, J. N., Clark, R. N., Annadurai, M., Boardman, J., Buratti, B., Combe, J.-P., Dyar, M. D., Green, R., Head, J. W., Hibbitts, C., Hicks, M., Isaacson, P., Klima, R., Kramer, G., Kumar, S., Livo, E., Lundeen, S., Malaret, E., . . . Varanasi, P. (2009). Character and Spatial Distribution of OH/H<sub>2</sub>O on the Surface of the Moon Seen by M<sup>3</sup> on Chandrayaan-1. *Science*, 326(5952), 568-572.  
<https://doi.org/10.1126/science.1178658>
- Pieters, C. M., Hanna, K. L. D., Cheek, L. C., Dhingra, D., Prissel, T. C., Jackson, C. R., Moriarty, D. P., Parman, S. W. & Taylor, L. A. (2014). The distribution of MG-spinel across the moon and constraints on crustal origin. *American Mineralogist*, 99(10), 1893–1910.  
<https://doi.org/10.2138/am-2014-4776>
- Prissel, T. C., & Prissel, K. B. (2021). A lunar sample renaissance. *Nature Communications*, 12(1), 7053.  
<https://doi.org/10.1038/s41467-021-27296-3>
- Potter, R. W. K., Head, J. W., Guo, D., Liu, J., & Xiao, L. (2018). The Apollo Peak-Ring Impact Basin: Insights into the structure and evolution of the South Pole–Aitken Basin. *Icarus*, 306, 139-149.  
<https://doi.org/10.1016/j.icarus.2018.02.007>
- Rouault, E., Warmerdam, F., Schwehr, K., Kiselev, A., Butler, H., Łoskot, M., Szekeres, T., Tourigny, E., Landa, M., Miara, I., Elliston, B., Chaitanya, K., Plesea, L., Morissette, D., Jolma, A., & Dawson, N. (2023). *GDAL* (v3.7.1) [Software]. Zenodo. <https://doi.org/10.5281/ZENODO.5884351>

- Sasaki, S., Iijima, Y., Tanaka, K., Kato, M., Hashimoto, M., Mizutani, H., & Takizawa, Y. (2003). The SELENE mission: Goals and status. *Advances in Space Research*, 31(11), 2335-2340.  
[https://doi.org/10.1016/S0273-1177\(03\)00543-X](https://doi.org/10.1016/S0273-1177(03)00543-X)
- Serventi, G., Carli, C., Sgavetti, M., Ciarniello, M., Capaccioni, F. & Pedrazzi, G. (2013). Spectral variability of plagioclase–mafic mixtures (1): effects of chemistry and modal abundance in reflectance spectra of rocks and mineral mixtures. *Icarus*, 226(1), 282–298.  
<https://doi.org/10.1016/j.icarus.2013.05.041>
- Shearer, C. K., Elardo, S. M., Petro, N. E., Borg, L. E., & McCubbin, F. M. (2015). Origin of the lunar highlands Mg-suite: An integrated petrology, geochemistry, chronology, and remote sensing perspective. *American Mineralogist*, 100(1), 294-325. <https://doi.org/10.2138/am-2015-4817>
- Shkuratov, Yu., Surkov, Ye., Ivanov, M., Korokhin, V., Kaydash, V., Videen, G., Pieters, C., & Stankevich, D. (2019). Improved Chandrayaan-1 M3 data: A northwest portion of the Aristarchus Plateau and contiguous maria. *Icarus*, 321, 34-49. <https://doi.org/10.1016/j.icarus.2018.11.002>
- Suarez-Valencia, J. E. (2024). Javierunal16/MoonIndex: Second version of the MoonIndex Python package (2.0.2) [Software]. Zenodo. <https://doi.org/10.5281/zenodo.10820503>
- Suarez-Valencia, J. E., Rossi, A. P., Zambon, F., Carli, C., & Nodjoumi, G. (2024). Supporting material for: MoonIndex, an Open-Source Tool to Generate Spectral Indexes for the Moon from M3 Data [Dataset]. Zenodo. <https://doi.org/10.5281/zenodo.10810407>
- Sunshine, J. M., & Pieters, C. M. (1998). Determining the composition of olivine from reflectance spectroscopy. *Journal of Geophysical Research: Planets*, 103(E6), 13675-13688.  
<https://doi.org/10.1029/98JE01217>
- Sunshine, J. M., Pieters, C. M., & Pratt, S. F. (1990). Deconvolution of mineral absorption bands: An improved approach. *Journal of Geophysical Research*, 95(B5), 6955.  
<https://doi.org/10.1029/JB095iB05p06955>
- Taylor, G. J. (1972). The composition of the lunar highlands: Evidence from modal and normative plagioclase contents in anorthositic lithic fragments and glasses. *Earth and Planetary Science Letters*, 16(2), 263-268. [https://doi.org/10.1016/0012-821X\(72\)90200-2](https://doi.org/10.1016/0012-821X(72)90200-2)
- Taylor, S. R. (1976). *Geochemical Constraints on the Composition of the Moon*. 7, 855.

- Warren, P. H. & Korotev, R. L. (2022). Ground truth constraints and remote sensing of Lunar Highland crust composition. *Meteoritics & Planetary Science*, 57(2), 527–557.  
<https://doi.org/10.1111/maps.13780>
- Wu, Y., Xue, B., Zhao, B., Lucey, P., Chen, J., Xu, X., Li, C., & Ouyang, Z. (2012). Global estimates of lunar iron and titanium contents from the Chang' E-1 IIM data: LUNAR Fe AND Ti FROM CHANG'E-1 IIM DATA. *Journal of Geophysical Research: Planets*, 117(E2), n/a-n/a.  
<https://doi.org/10.1029/2011JE003879>
- Zambon, F., Carli, C., Altieri, F., Luzzi, E., Combe, J.-P., Ferrari, S., Tognon, G., & Massironi, M. (2020). *Spectral Index and RGB maps—Beethoven, Rembrandt basins on Mercury, Apollo basin and Leibnitz and Von Karman craters regions on the Moon* (p. 57).
- Zhang, L., Dong, W., Zhang, D., & Shi, G. (2010). Two-stage image denoising by principal component analysis with local pixel grouping. *Pattern Recognition*, 43(4), 1531-1549.  
<https://doi.org/10.1016/j.patcog.2009.09.023>
- Zhang, X.-Y., Ouyang, Z.-Y., Zhang, X.-M., Chen, Y., Tang, X., Xu, A.-A., Tang, Z.-S., & Wu, Y.-Z. (2016). Study of the continuum removal method for the Moon Mineralogy Mapper ( $M^3$ ) and its application to Mare Humorum and Mare Nubium. *Research in Astronomy and Astrophysics*, 16(7), 015. <https://doi.org/10.1088/1674-4527/16/7/115>
- Xu, J., Mo, B., Wu, Y., Zhao, Y., Lin, H., Ye, B., Michalski, J. R., Li, Y., Tai, K., Li, C., Guo, Z., Qi, C., Liu, S., Li, X. & Liu, J. (2023). Space weathering effects and potential spectral alteration on Phobos and the moon: clues from the FE content of Olivine. *Astronomy and Astrophysics*, 672, A115.  
<https://doi.org/10.1051/0004-6361/202245453>

Supporting Information for

## **MoonIndex, an Open-Source Tool to Generate Spectral Indexes for the Moon from M3 Data**

**Javier Eduardo Suárez-Valencia<sup>1</sup>, Angelo Pio Rossi<sup>1</sup>, Francesca Zambon<sup>2</sup>, Cristian Carli<sup>2</sup>, and Giacomo Nodjoumi<sup>1</sup>**

<sup>1</sup>School of Science, Constructor University, Bremen, Germany, <sup>2</sup>INAF-Istituto Nazionale di Astrofisica, Italy.

## Contents of this file

Text S1 to S2  
Figures S1 to S2

## Introduction

In this supplementary material we detail the preparation of the data before being ingested to ***MoonIndex***, and the libraries used in python to generate the spectral indexes. Since the code to process the data in ISIS is not included on ***MoonIndex***, we will show the workflow we followed to map-project the images. Furthermore, we showcase 24 indexes resulting from our workflow, we show only the images obtained by the convex hull continuum-removal method, since it was the one used in the main text. For an explanation about the meaning of the indexes, refer to **Table 1** in the main text. The map-projected M<sup>3</sup> data cubes and the resulting indexes for the Apollo basin, Vallis Alpes, and Aristarchus crater can be found in this zenodo repository:

<https://zenodo.org/records/10014564>.

## Text S1.

The preprocessing of the data in ISIS consists on the map-projection of the cubes to a predefined coordinate system. ISIS does not recognize the higher-processed reflectance cube as an input, so the radiance cubes and associated files also need to be used. Before the projection could be done, we changed the name of the radiance cube by the one of the reflectance cube in the LBL file, this is done in the “^RDN\_IMAGE” parameter under the “/\* Spectral calibration parameters and radiometric gain factor data \*/” section of the file (**Figure S2**).

```
55
56 /* Spectral calibration parameters and radiometric gain factor data */
57
58 CH1:SPECTRAL_CALIBRATION_FILE_NAME = "M3G20081211_RDN_SPC.TAB"
59 CH1:RAD_GAIN_FACTOR_FILE_NAME     = "M3G20081211_RDN_GAIN.TAB"
60 CH1:GLOBAL_BANDPASS_FILE_NAME    = "M3G20081211_RDN_BPF.IMG"
61
62 /* Description of Radiance-corrected image file */
63
64 OBJECT = RDN_FILE
65 ^RDN_IMAGE = "M3G20090204T192552_V03_RDN.IMG"
66 RECORD_TYPE = FIXED_LENGTH
67 RECORD_BYTES = 103360
68 FILE_RECORDS = 18593
69
70 OBJECT = RDN_IMAGE
71 LINES = 18593
72 LINE_SAMPLES = 304
73 SAMPLE_TYPE = PC_REAL
74 SAMPLE_BITS = 32
75 UNIT = "W/(m^2 um sr)"
76 BANDS = 85
77 BAND_STORAGE_TYPE = LINE_INTERLEAVED
78 LINE_DISPLAY_DIRECTION = DOWN
79 SAMPLE_DISPLAY_DIRECTION = RIGHT
80 END_OBJECT = RDN_IMAGE
81
82 END_OBJECT = RDN_FILE
83
```

**Figure S1.** Replacement of names on the radiance LBL file.

Once the replacement has been done, the full processing on ISIS and GDAL can be done with the following bash commands:

### ***Listing all files to do the batch processing***

```
ls *V03_L1B.LBL | sed s/_L1B.LBL// > Imputs.lis
```

### ***Transformation from IMG to cubes***

```
chan1m32isis from=\$1_L1B.LBL loc=\$1_LOC.IMG obs=\$1_OBS.IMG  
to=\$1.cub -batchlist=Imputs.lis
```

### ***Actualization of cubes kernels***

```
spiceinit from=\$1.cub -batchlist=Imputs.lis
```

### ***Making a new list***

```
ls *V03.cub | sed s/.cub// > Imputs2.lis
```

### ***Map projection, a map template need to be previously created***

```
cam2map from=\$1.cub map=M3.map to=\$1_lv2.cub PIXRES=map -  
batchlist=Imputs2.lis
```

### ***Streth***

```
stretch from=\$1_lv2.cub to=\$1_lv2_nonull.cub NULL=65535 -  
batchlist=Imputs2.lis
```

### ***Listing all files***

```
ls *.cub | sed s/.cub// > Imputs.lis
```

### ***Translate***

```
for f in *_nonull.cub; do  
gdal_translate -a_nodata 65535 "$f" "${f%.*}.tif"  
done
```

Once these commands have been run, the cubes will be projected and in .TIF format, and ready to ingest on ***MoonIndex***.

### ***Text S2.***

We used several python libraries during our workflow. Here we will discuss the application of all of them, and the full code can be access via the GitHub repository (<https://github.com/Javierunal16/MoonIndex>).

**Preparation:** During the preparation we used *rioxarray* to open the data cubes, and *numpy* to open the text file with the wavelengths for each M<sup>3</sup> channel. Then, *matplotlib.patches* is required to clip the cube to the desired extent, and *matplotlib.pyplot* to graph the data. In the RGB composites we used *sklearn.preprocessing* to normalize the values before plotting.

**Filtering:** To filter the cube we rely on libraries designed for image processing. First, *cv2* and *numpy* were needed to apply the Fourier filtration. And later, *numpy*, *specutils* and *astropy* were used to apply the 1D Gaussian filter.

**Continuum removal:** We tried several option to apply the convex hull to the spectra, but we ended up using *numpy* and *scipy.signal* to find the midpoint and to calculate the convex hull. As for the second-and-first-order fit method, only *numpy* was needed.

**Indexes generation:** The creation of indexes is straightforward after the continuum removal, most of them require band operations that can be covered by *numpy*.

**Deployment:** The code was compiled using *wheel* and uploaded to PyPI with *twine*.

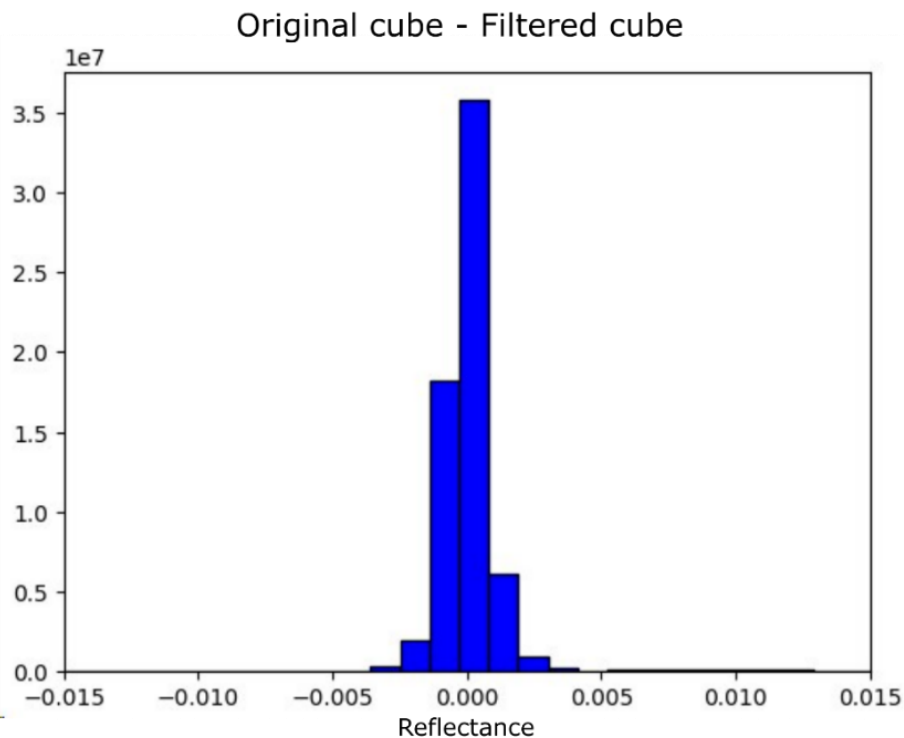


**Figure S2.** Distribution of the noise values for the Apollo basin cube for all the wavelengths. The values were obtained by subtracting the filtered cube to the unfiltered one. Most of the noise values are lower than 0.005 (which is well below the usual values of the band depth), so the detection limit of the band depth must be greater than this value.

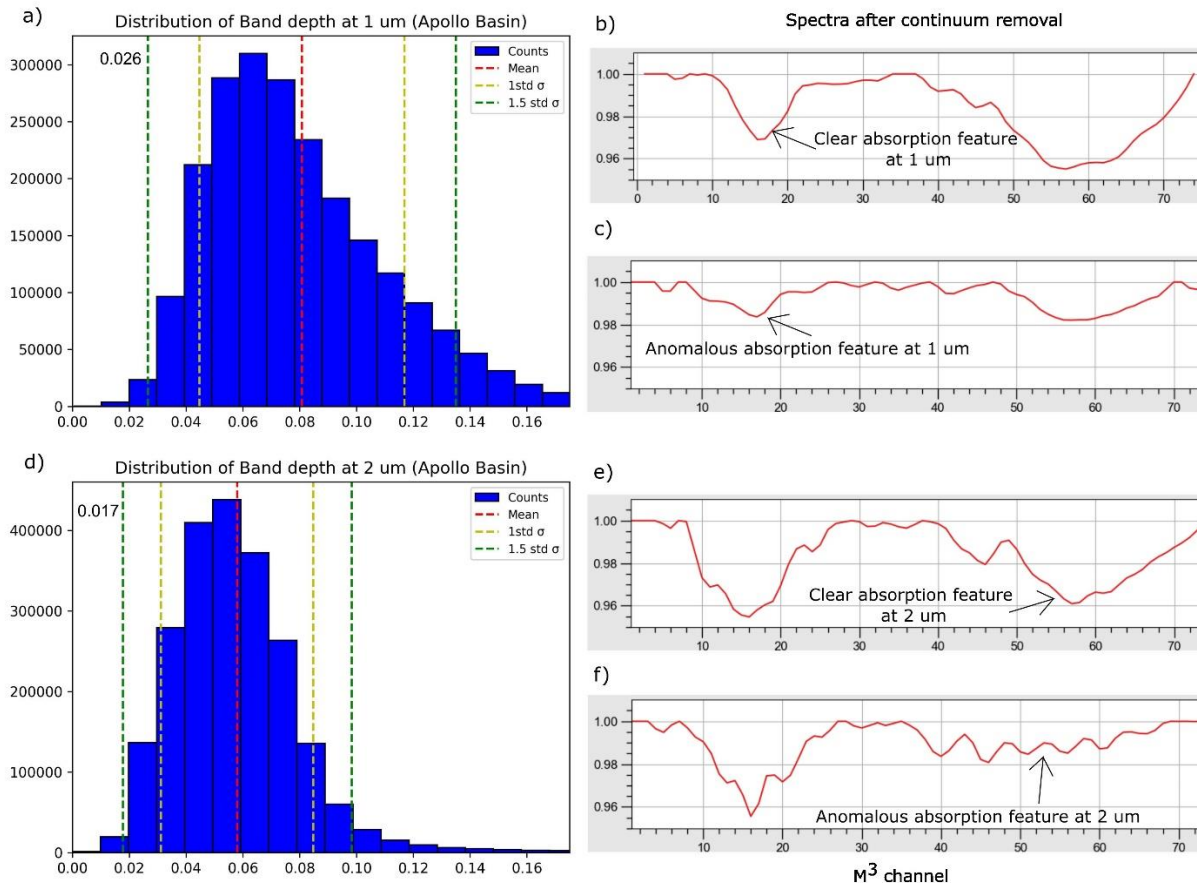
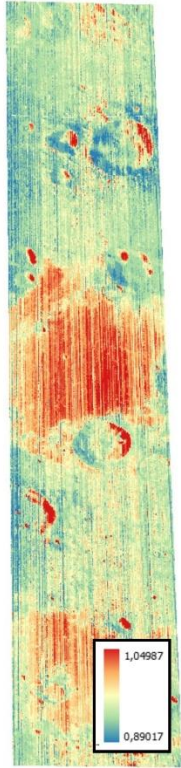


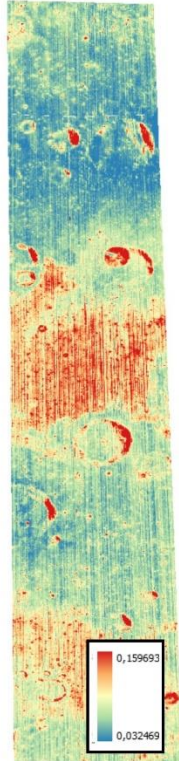
**Figure S3.** The Apollo basin covers highlands and mare terrains, representing the major mineralogical variations on the Moon, for this reason this cube was selected to define a detection limit for the calculation of the band depths. a) Distribution of the band depth at 1  $\mu\text{m}$ , after 1.5 standard deviations to the left (0.026), 0.16% of the pixels are filtered. b) Sample spectrum over the 0.025 limit, the absorption band at 1  $\mu\text{m}$  is well defined. c) Sample spectrum below the 0.026 limit, the absorption band is anomalous. b) Same for the band depth at 2  $\mu\text{m}$ , in this case below 0.017, 0.35% of the pixels are filtered. e) Sample spectrum over the 0.017 limit, the absorption is well defined, f) Sample example below the 0.017 limit, the absorption is anomalous.



R540



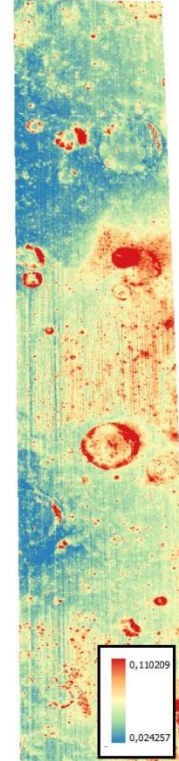
BCI



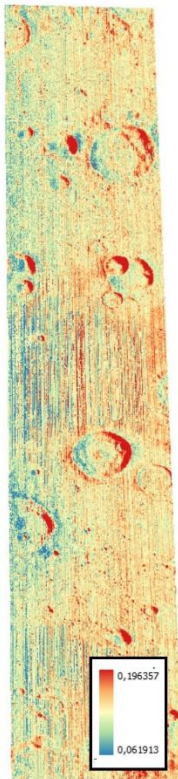
BDI



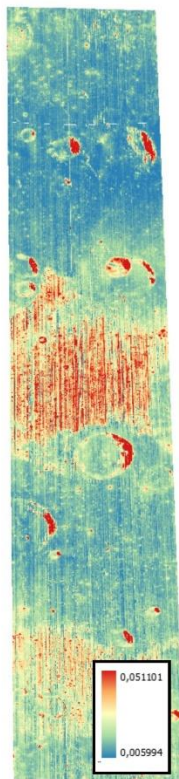
BCII



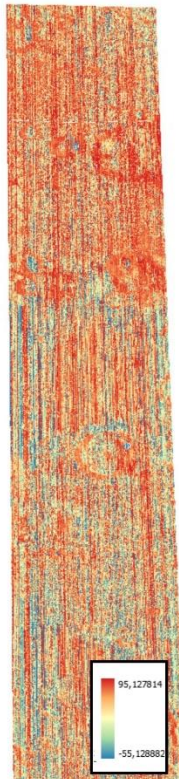
BDII



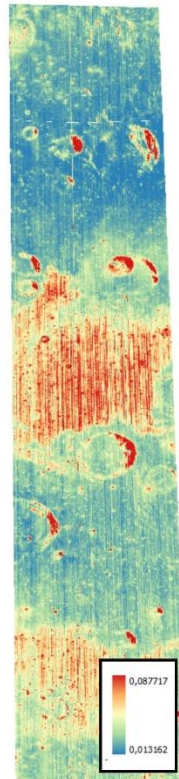
SS



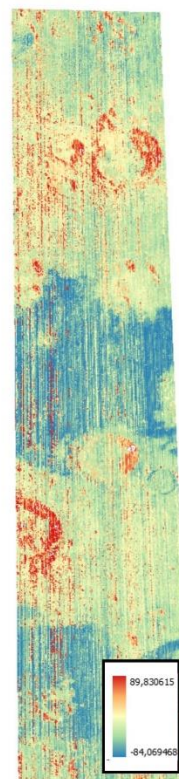
BAI



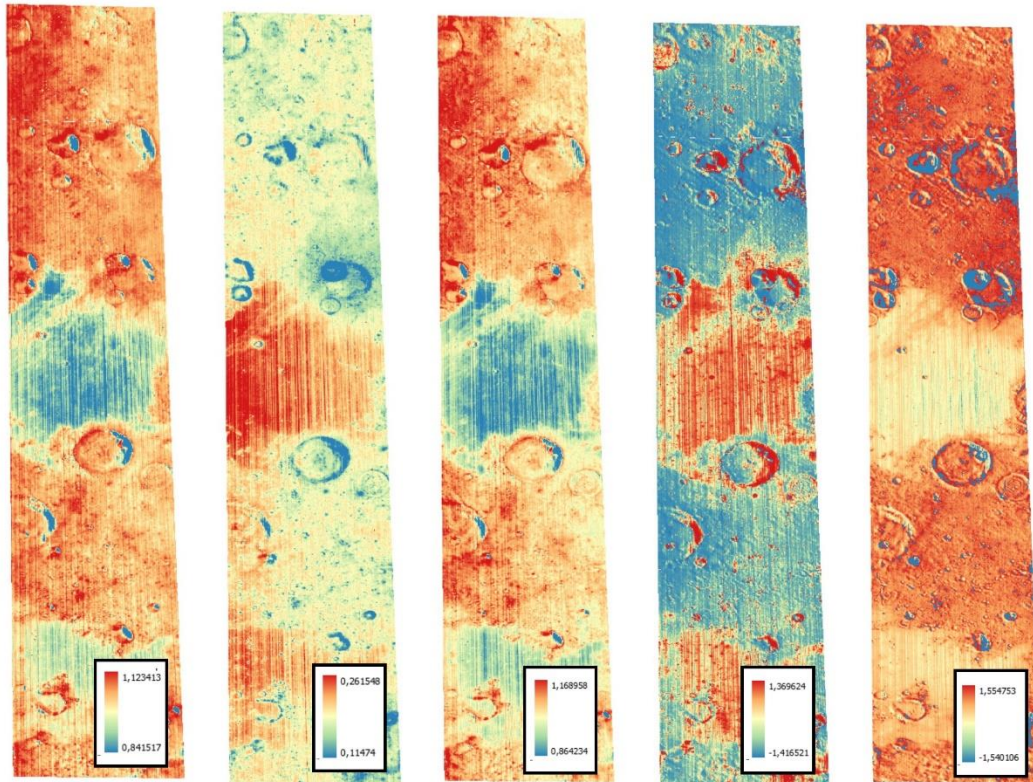
ASYI



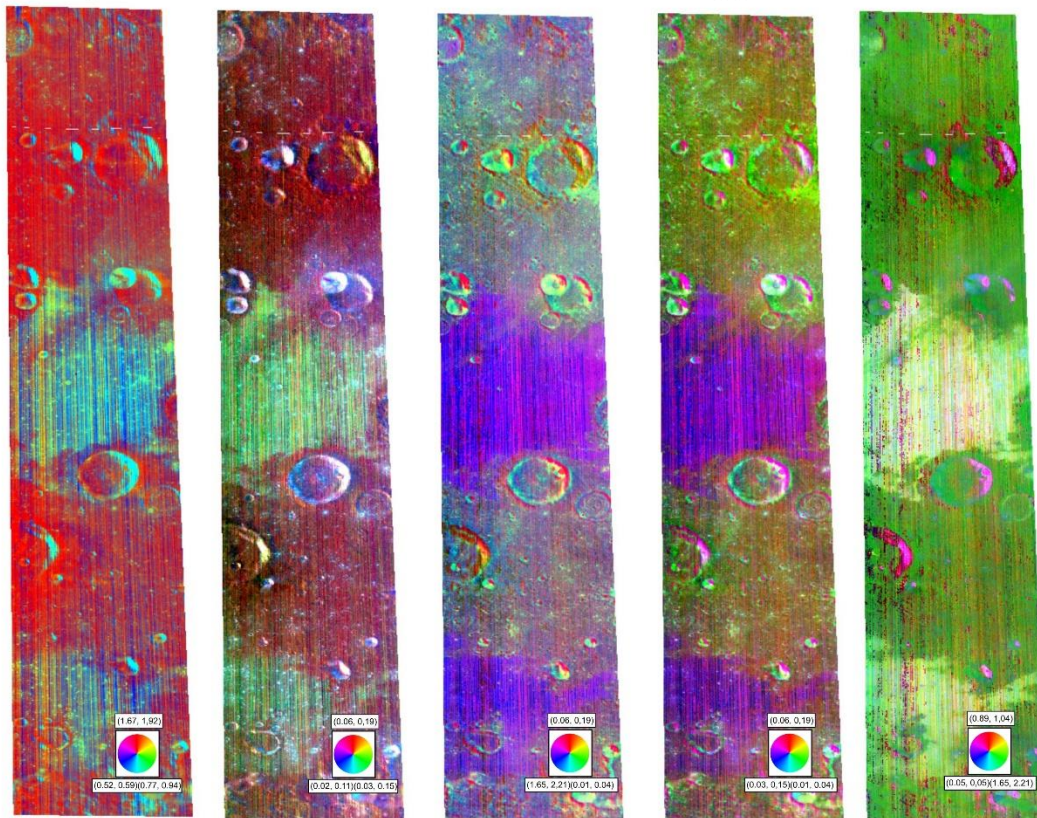
BAII



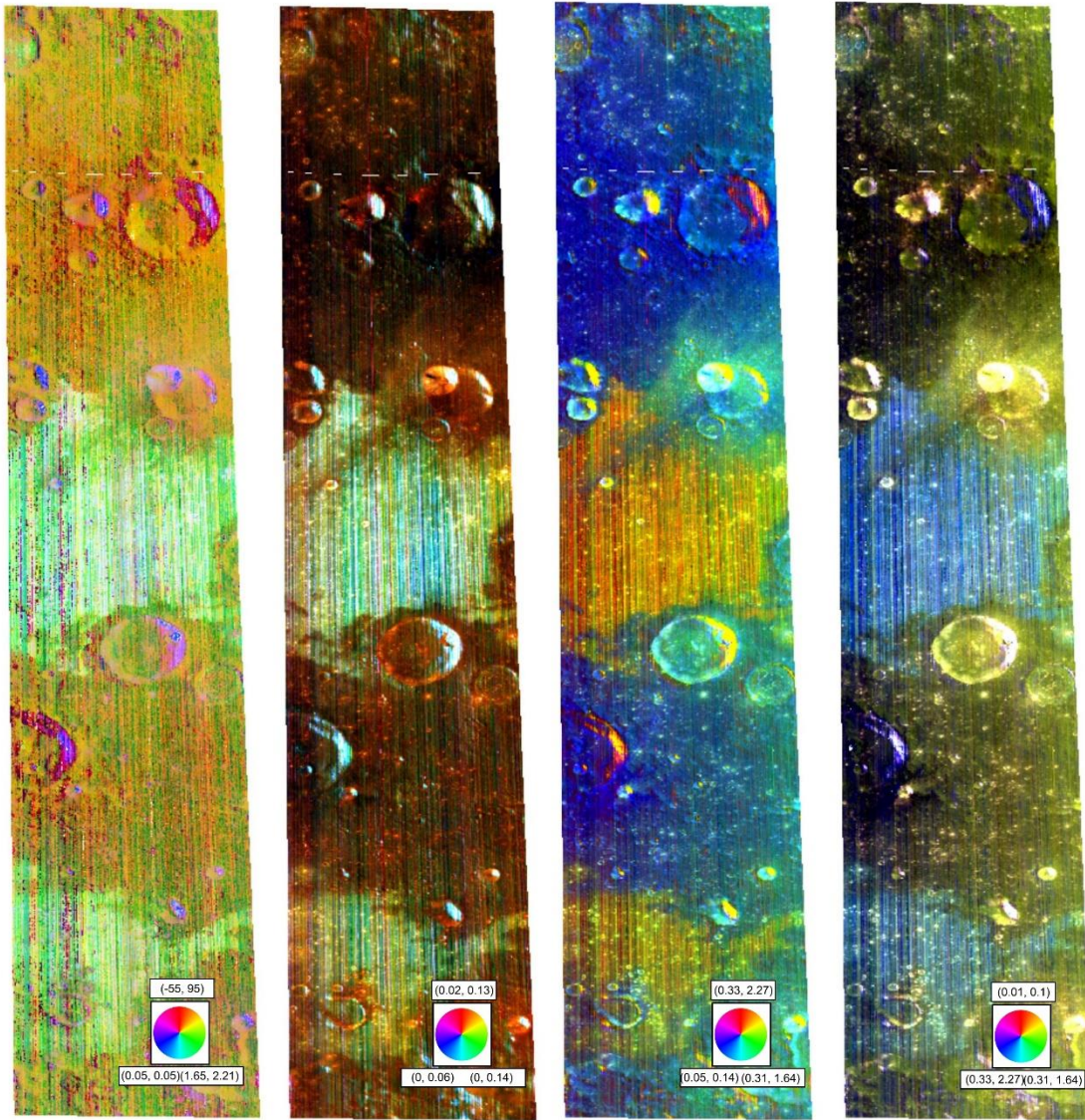
ASYII



Sp Ol Cr Fe Ti



Clem RGB1 RGB2 RGB3 RGB4



RGB5

RGB6

RGB7

RGB8

3

4 **Figure S4.** Spectral indexes derived from *MoonIndex* in the Apollo basin, using the convex-hull  
 5 method.

6